Position and Attitude Model-Based Thruster Fault Diagnosis: A Comparison Study

Robert Fonod, David Henry, Catherine Charbonnel, Eric Bornschlegl

Position and Attitude Model-Based Thruster Fault Diagnosis: A Comparison Study

Robert Fonod[1] and David Henry[2]
University of Bordeaux, 33405 Talence, France

Catherine Charbonnel[3]
Thales Alenia Space, 06156 Cannes la Bocca, France

Eric Bornschlegl[4]
European Space Agency, 2200 AG Noordwijk, The Netherlands

This paper deals with performance and reliability evaluation of a fault diagnosis scheme based on two distinct models to detect and isolate a single thruster fault affecting a chasing spacecraft during rendezvous with a passive target in a circular orbit. The analysis is conducted in the frame of a terminal rendezvous sequence of the Mars Sample Return mission. A complete description of a robust residual generation design approach based on eigenstructure assignment is presented.Unknowntime-varying delays, induced by the thruster drive electronics and uncertainties on thruster rise times, are considered as unknown inputs. Particular novelty of the work is a new method for estimating the unknown input directions used to enhance the robustness properties of the diagnosis scheme. Monte Carlo results from a high-fidelity industrial simulator and carefully selected performance and reliability indices allows us to evaluate the effectiveness of both schemes. The obtained results reveal that the proposed fault diagnosis scheme based on a position model is a justified competitor to the conventionally used attitude model-based scheme.

---

[1] Ph.D. Candidate, Automatic Control Group, IMS (Intégration du Matériau au Système) Laboratory - UMR CNRS 5218, 351 Cours de la Libération; robert.fonod@ims-bordeaux.fr (Corresponding Author).
[2] Professor, Automatic Control Group, IMS (Intégration du Matériau au Système) Laboratory - UMR CNRS 5218, 351 Cours de la Libération;
[3] GNC Senior Research Engineer, Research Department - DRT/SO, 5 allée des Gabians.
[4] GNC System and Avionics Engineer, ESTEC (European Space Research and Technology Centre), TEC-ECN, Keplerlaan 1, P.O. Box 299.

Nomenclature

$\boldsymbol{A}$ (bold capital letters)	= matrices
a	= radius of the target's circular orbit (m)
c (normal lowercase letters)	= scalars
$\boldsymbol{C}$	= torque vector (N·m)
$\boldsymbol{F}$	= force vector (N)
$\boldsymbol{f}$	= additive fault vector
$\boldsymbol{I}$, $\boldsymbol{0}$	= identity and null matrix with appropriate dimensions
$\boldsymbol{I}_n$	= $n \times n$ identity matrix
$\boldsymbol{I}_{chs}$	= inertia matrix (kg·m^2)
$\boldsymbol{M}$	= thruster configuration matrix
m	= mass (kg)
$\hat{m}_{loss}$, $\hat{m}_{leak}$	= thrust loss size and maximum leakage size
n	= orbital rate of the target (rad·s^{-1})
p, q, r	= roll, pitch, and yaw rate (rad·s^{-1})
$\hat{Q}_{tgt}$, $\hat{Q}_{chs}$	= quaternion estimates describing the orientation of the target and chaser with respect to the Mars-centered inertial frame
$\boldsymbol{r}$, r	= vector of residuals and scalar residual
T	= sampling interval (s)
T_{on_i}	= scaled open duration of the ith thruster
$\vec{\boldsymbol{X}}, \vec{\boldsymbol{Y}}, \vec{\boldsymbol{Z}}$	= mutually perpendicular (orthogonal) unit vectors
$\boldsymbol{x}$ (bold lowercase letters)	= vectors
ξ, η, ζ	= Cartesian component of the relative position (m)
φ, θ, ψ	= roll, pitch, and yaw angle (rad)
$\boldsymbol{\Lambda}(\boldsymbol{A})$	= set of all eigenvalues of a matrix $\boldsymbol{A}$
$\tau(t)$	= time-varying delay (s)
$\mathbb{R}$, $\mathbb{Z}^+$	= field of real numbers and set of non-negative integers
$\mathcal{R}_l, \mathcal{R}_i, \mathcal{R}_b$	= local (target), Mars-centered inertial, and chaser body-fixed reference frame

$\|\cdot\|, \|\cdot\|_F$	= Euclidean norm (vectors) and Frobenius norm (matrices)
Subscripts	
a	= attitude model
p	= position model
f	= outlines the faulty case
Superscripts	
M	= Mars planet
f	= outlines the faulty case

I. Introduction

Many space exploration missions require critical autonomous proximity operations. Mission safety is usually guaranteed through a hierarchical implementation of fault/failure detection, isolation and recovery (FDIR) approach with several levels of fault containments defined from local component/equipment up to global system, i.e., through various equipments (sensors, thrusters, reaction wheels etc.) redundancy paths and ground intervention [1–3]. In the case of the Mars Sample Return (MSR) mission, the hierarchical implementation of FDIR is concerned at three levels [4, 5]: (i) based exclusively on sensor measurements in the fault detection and isolation (FDI) function which are mainly signal-based techniques, (ii) relying on both actuator commands and sensor measurements in the model-based FDI function, and (iii) based on navigation outputs for the monitoring of the trajectory in the safety monitoring function. Through this hierarchical strategy, it is assumed that sensor faults are diagnosed and recovered at the first level. This paper focuses on the second level of this hierarchy. The goal is to develop a robust model-based FDI unit for faults occurring in the spacecraft involved in the MSR mission.

Common FDIR techniques may be not sufficient in some cases, especially for faulty situations that cause quickly abnormal dynamics deviation in critical space operations. This is especially the case during rendezvous and docking/capture proximity operations. Advanced model-based FDI techniques should be particularly developed to safely accommodate on-board (and on-line) the necessary robustness/stability of the spacecraft control, the necessary trajectory dynamics and the

vehicle nominal operation.

To ensure normal operation, real-time fault diagnosis is essential to provide information for the spacecraft to accommodate the fault in time. Numerous model-based FDI techniques are reported in the literature and have potential to be applied [6–9]. The problem of thruster faults is however less studied. Among other examples, methods based on the so-called unknown input observer (UIO) technique were applied to the Mars Express mission [11, 12]; an iterative learning observer (ILO) was designed to achieve estimation of time-varying thruster faults [10]; H_∞/H_- filters were used to addresses the problem of thruster fault diagnosis in the Microscope satellite [13] and also the problem of faults affecting the micro-Newton colloidal thrust system of the LISA Pathfinder experiment [14]. Both H_∞/H_- filters are based on a residual generator, that is robust against spatial disturbances (e.g., J_2 disturbances, atmospheric drag and solar radiation), measurement noises and sensor misalignment phenomena, whilst guaranteeing some fault sensitivity performance.

On the other hand, only limited results on FDI of time-delay systems have been developed in recent years in the literature. Among the contributions, an UIO was designed for fault detection of state-delayed systems with known delays [15]. The well known parity space approach was extended for fault detection of retarded time-delay systems [16]. Two-objective optimization approach was considered for linear time-invariant (LTI) systems with constant time delays aiming at formulation of the optimization problem as: enhancing sensitivity of the residual to faults and at the same time suppressing the undesirable effects of unknown inputs and uncertainties in $\mathcal{L}_2$-gain sense [17, 18]. Robust fault diagnosis approach based on an adaptive observer was developed for uncertain continuous LTI systems with multiple discrete time-delays in both states and outputs [19]. Recently, a geometric approach for FDI of retarded and neutral time-delay systems was developed [20]. Problem of robust fault detector design for a class of LTI systems with some nonlinear perturbations and mixed neutral and discrete time-varying delays was investigated using a descriptor technique, Lyapunov-Krasovskii functional and a suitable change of variables [21].

Often, uncertain time-varying delays occurs in the input channel of the system. Considering spacecraft's thrusters, such delays may be induced by the propulsion drive electronics. One of the main difficulty in fault diagnosis of systems with uncertain input delays lies in the fact that

uncertainty caused by this delay is unstructured. Therefore, robustness cannot be achieved by applying existing robust unknown input (disturbance) decoupling approaches directly. There is an important assumption for all such approaches that the disturbance distribution matrix must be known, but a generalized approach to obtain the matrix is still lacking [22, 23].

One possible solution to this problem is to transform the unstructured input uncertainty to unknown input by means of time-dependent Padé approximation [24]. In this paper, we have taken an approach similar to [25], where by introducing a Cayley-Hamilton theorem-based and h-order Taylor series expansion-based polytopic transformations, the influence/uncertainty of the time-varying delay on the system is summarized as an unknown input. By assigning the eigenstructure of the observer, the residuals can be decoupled from these unknown inputs [22]. The solutions investigated in this paper follow this strategy. Two FDI schemes are proposed based on two different models of the spacecraft dynamics, i.e., the so-called position model scheduled by judiciously chosen parameters, which exhibit the translation dynamic of the spacecraft in a judiciously chosen frame, and the attitude model.

The position model expressed in the local reference frame is well known and mastered for control, but rarely used for FDI of thrusters. The reason is quite evident, the attitude model seems to be more sensitive to thruster faults. The innovation that we pursue with this study is concerning the judiciously chosen position model for FDI and its comparison to the attitude model-based solution.

Simulation results from "high-fidelity" MSR industrial simulator, under realistic conditions and taking into account the effects that the GNC (Guidance, Navigation, Control) unit has on the FDI performances, demonstrate the efficiency and capabilities of the proposed methodology. These two FDI schemes have been successfully demonstrated as applicable for FDI of the chaser spacecraft involved in the MSR mission within the critical dynamics and operation constraints of the last terminal translation of the rendezvous/capture phase. The research work presented in this paper draws expertise from actions undertaken within the European Space Agency (ESA), Thales Alenia Space and the IMS laboratory (University of Bordeaux). The aim is to demonstrate the benefits of novel robust on-board FDI technologies, that may significantly enhance the spacecraft autonomy.

The paper is organized as follows: Section II briefly describes the MSR mission and introduces

the modeling of the chaser spacecraft propulsion and control system. Necessities of modeling the spacecraft dynamics during the rendezvous phase are recalled in Sec. III. Section IV addresses the theoretical basements and computational procedure of the FDI scheme design. For a detailed assessment of the FDI performances, results of the Monte Carlo simulation campaign incorporating different fault scenarios are presented in Sec. V. Finally, some concluding remarks are given in Sec. VI.

II. Background

A. Overview of the MSR mission

The MSR mission is one of the most exciting challenges in the international effort on the Solar System exploration. The mission concepts have been studied for years by NASA [26], French National Space Agency (CNES) [27], and ESA. Its main goal is to collect samples of Martian rocks, soils and atmosphere, and to return these samples safe and intact back to Earth for analysis.

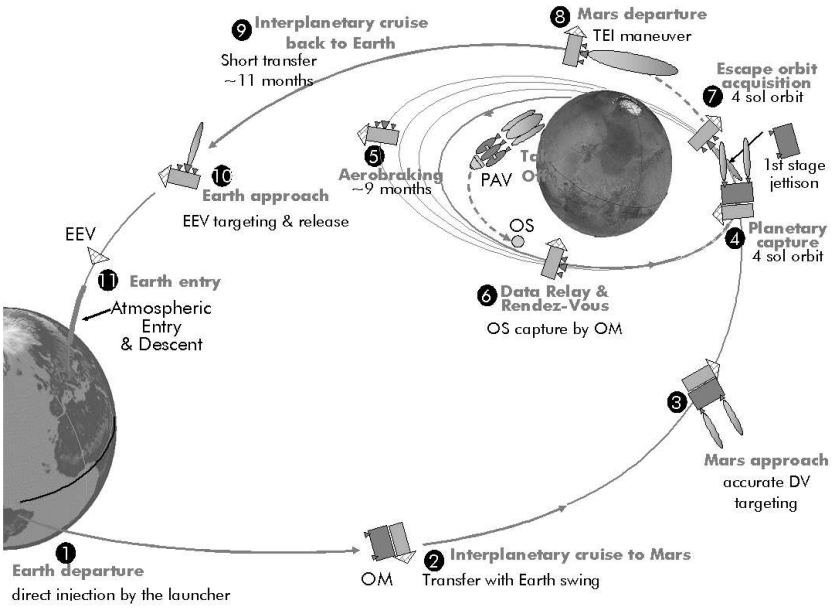

Fig. 1 Illustration of the MSR mission.

This mission consists of two spacecrafts directly injected towards Mars by launchers [28]. The descent module is released on the Martian atmosphere (Entry phase), lands on the Mars surface and a rover vehicle is released. Once the rover finished the collecting procedure, the samples are put

into the sample container and loaded on the Mars ascent vehicle (MAV) which is then launched, by means of rockets, into a low Mars orbit. Meanwhile the second module, the Earth-return vehicle (chaser), is injected towards the Mars planet to rendezvous with the sample container (target) and bring it back to Earth. The chaser achieves the sample capture as soon as it is released by the MAV, which performs the last maneuver in order to avoid any interference with the rendezvous operation. Finally, after successful capture, the sample container is inserted into an Earth re-entry capsule (ERC) inside the chaser vehicle and the chaser starts its interplanetary cruise towards the Earth. It should be noted, that this autonomous capture maneuver belongs to the non-cooperative rendezvous since the target is not equipped with any actuation system. Figure 1 provides an overview of the mission. The work addressed in this paper concerns the last 20m of the rendezvous phase.

B. Chaser Spacecraft Configuration

Figure 2 shows the general setup of the GNC system in the chaser vehicle (for confidential reasons, the numerical values with regards to the spacecraft geometry and characteristics are omitted).

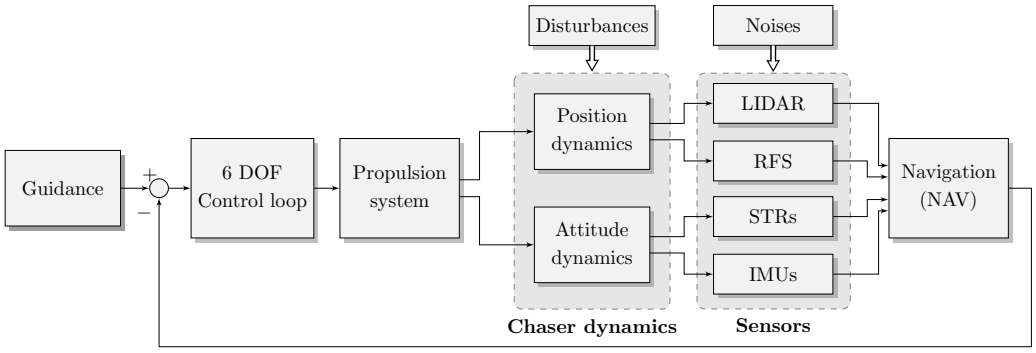

Fig. 2 General setup of the chaser's GNC system during the rendezvous.

The selected attitude and orbital control system dedicated to spacecraft mode for the rendezvous phase corresponds to 6 degree of freedom (DOF) control. The 6 DOF control ensures the application of both commanded torque and force using thrusters only.

The control system relies on the following sensors:

- 2 3-axis inertial measurement unit (IMU) in hot redundancy;
- 2 star trackers (STR) in cold redundancy;

- 2 short-range rendezvous sensors with a functional hot redundancy, i.e., a light detection and ranging (LIDAR) sensor and a radio frequency sensor (RFS) as back-up.

The IMU unit is in charge of measuring the angular velocities $\boldsymbol{\omega} = [p, q, r]^T$. The STR device gives the attitude measurement $\boldsymbol{\Theta} = [\varphi, \theta, \psi]^T$. The LIDAR unit is in charge of the measurement of the relative position $\boldsymbol{\rho} = [\xi, \eta, \zeta]^T$ between the chaser and target. The RFS sensor is used to monitor the chaser trajectory, and it can trigger a collision avoidance maneuver, if necessary.

The role of the navigation (NAV) unit is to perform an estimate $\hat{\boldsymbol{\Theta}}, \hat{\boldsymbol{\omega}}, \hat{\boldsymbol{\rho}}$ of $\boldsymbol{\Theta}, \boldsymbol{\omega}, \boldsymbol{\rho}$, respectively, by removing the misalignment phenomena, sensor bias and noises on these measurements. The NAV unit also provides an estimate of the target attitude quaternion $\hat{\boldsymbol{Q}}_{tgt}$, that will be used later for the design of the FDI unit. However, we assume that the NAV unit is not perfect and, thus, that there still exists time delays and noises on $\hat{\boldsymbol{\Theta}}, \hat{\boldsymbol{\omega}}, \hat{\boldsymbol{\rho}}$, and $\hat{\boldsymbol{Q}}_{tgt}$, respectively.

In terms of actuators, the chaser vehicle is equipped with a very precise chemical propulsion system composed of 16 thrusters (THR) in full redundancy. They are organized in two sets, the nominal set 'A' is used for the nominal vehicle control and the redundant set 'B' is reserved for the recovery actions after a fault has been detected in the active set. The thruster configuration is illustrated in Fig. 3.

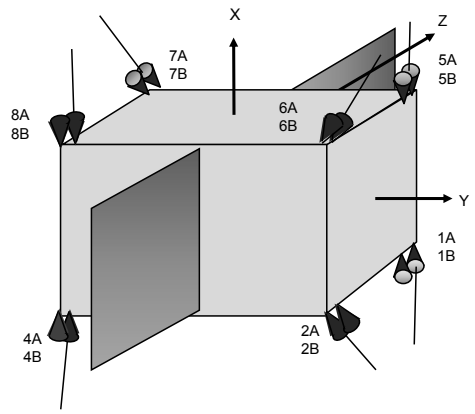

Fig. 3 Thruster configuration of the chaser spacecraft.

C. Modeling the Control Loop and the Propulsion System

To carry out its mission and to ensure the mission performance, the chaser is equipped with 6 DOF control law, see Fig. 4 for an illustration. It consists of two dynamic controllers: $\boldsymbol{K}_{pos}(s)$

that is in charge of controlling the position dynamics and $\boldsymbol{K}_{att}(s)$ that aims to regulate the chaser's attitude. The controller outputs, the desired force $\boldsymbol{F}_d$ and the desired torque $\boldsymbol{C}_d$, are sent to the thruster modulator unit (TMU) that integrates the small commanded pulses which are below the minimum impulse bit (MIB) and releases a pulse ($\widetilde{\boldsymbol{F}}_d$ or/and $\widetilde{\boldsymbol{C}}_d$) when the total reaches a momentum threshold. The TMU is widely used to compensate the actuator nonlinearities and improve the control accuracy [4, 29]. The purpose of on-board thruster management function (TMF) is to select specific thrusters and compute their firing times T_{on_i} to realize force $\widetilde{\boldsymbol{F}}_d$ and torque $\widetilde{\boldsymbol{C}}_d$ command impulses coming from the TMU. The TMF algorithm relies on a simplified approach with respect to the Simplex and thrusters' non-linearities (minimum On/Off times) [4].

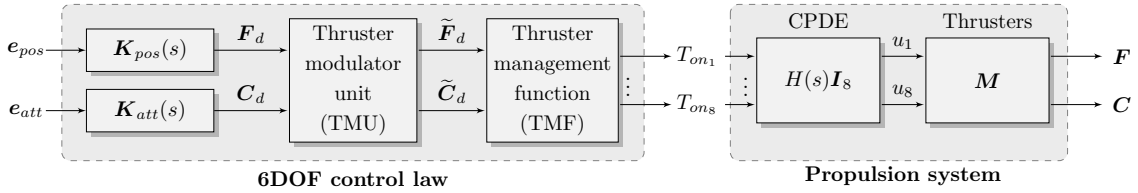

Fig. 4 Control architecture of the thruster-based propulsion system of the chaser vehicle.

As mentioned earlier, the propulsion system uses only 8 of the 16 thrusters in the nominal case thus, in the following, we are focusing on these 8 thrusters. The thrusters have fixed directions and each one is able to produce a maximum thrust of 22N. The chemical propulsion drive electronics (CPDE), that drives the thrusting actuators, is initiating the opening of the thruster valve for the commanded duration $0 \leq T_{on_i} \leq 1, i = 1, \ldots, 8$. T_{on_i} are scaled on-times. The scaling is done versus the sampling period T of the control unit and is defined according to $T_{on_i} = \bar{T}_{on_i}/T$, $\bar{T}_{on_i}$ being the actual/real firing time.

The propulsion system is a source of uncertainty in the system. The linear parameter-varying transfer function

$$H(s) = e^{-\tau(t)s} \tag{1}$$

aims to model the effect of the unknown time-varying delays $\tau(t) \in \mathbb{R}$ induced by the CPDE electronic device and the uncertainties on the thruster rise times [30]. In the following, it is assumed that each thruster open duration $T_{on_i}, i = 1, \ldots, 8$ is delayed with the same delay $\tau(t)$. This is a

reasonable assumption from the practical point of view, since for all nominal thrusters the same CPDE device is used to control the opening of the thruster valve.

Let $T_{on_i}\big(t-\tau(t)\big)$ be the commanded open duration of the ith thruster delayed by $\tau(t)$, then the force vector $\boldsymbol{F}_{thr}=[F_\xi, F_\eta, F_\zeta]^T$ and the torque vector $\boldsymbol{C}_{thr}=[C_\varphi, C_\theta, C_\psi]^T$, generated by the thrusters, are given by

$$\begin{pmatrix} \boldsymbol{F}_{thr}(t) \\ \boldsymbol{C}_{thr}(t) \end{pmatrix} = \boldsymbol{M}\boldsymbol{T}_{on}\big(t-\tau(t)\big) \tag{2}$$

where $\boldsymbol{T}_{on}=[T_{on_1},\ \ldots,\ T_{on_8}]^T$ and $\boldsymbol{M}\in\mathbb{R}^{6\times 8}$ is the thruster configuration matrix. The elements of $\boldsymbol{M}$ are the influence coefficients defining how each thruster affects each component of $\boldsymbol{F}_{thr}$ and $\boldsymbol{C}_{thr}$, respectively.

D. Fault Considerations

It is obvious, that if a thruster fault occurs, for instance a hardover-type failure (thruster stuck open), it could lead to a drastic increase of the propellant consumption which is already very constrained by the travel to Mars. Dramatic consequences can occur, e.g., already in-placed GNC may not compensate such faults, possibly leading the chaser to lose the attitude and/or the position of the sample container. The problem becomes highly critical during the last 20 meters of the rendezvous phase when the chaser shall be correctly positioned in the rendezvous corridor (see Fig. 5 for illustration) in order to successfully capture the sample container as well as the chaser's attitude need to be maintained in the rendezvous sensor field of view.

Such faulty situations obviously cannot be diagnosed by ground support using telemetry information, due to the potential lack of communication between the chaser and the ground stations or due to significant communication delay. This motivates ESA to manage studies for the development of on-board fully autonomous FDI solutions that shall cope with all the failures which may occur and endanger the mission. A quick detection and isolation of the fault is the first step towards an efficient recovery action that has no impact on the mission success.

Through monitoring the sensor outputs, most of the faults in the chaser spacecraft can be

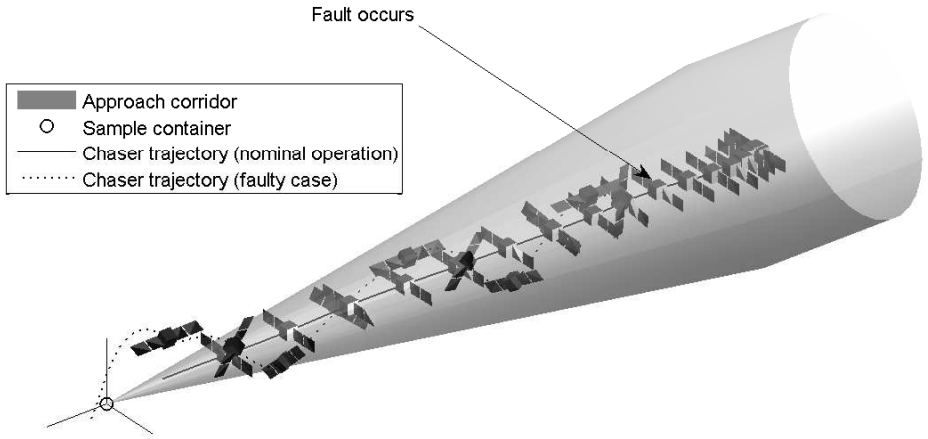

Fig. 5 The MSR rendezvous corridor.

detected at sensor data processing level (health status, operational mode, continuity checks, etc.) and recovery from these faults is usually quick enough, i.e., switching to a redundant sensor in hot redundancy (IMU case), or propagation of last valid measurement during the switch-on of the redundant equipment in cold redundancy (STR case). Most space agencies (NASA, ESA, CNES) have already identified LIDAR as a preferred candidate instrument for autonomous rendezvous. It seems to be a justified and robust device for the mission success [31]. Moreover, the problem of fault diagnosis of multiple sensor faults occurring in the chaser spacecraft has been already addressed in the literature [32]. Thus, the focus of this study concerns only thruster fault diagnosis.

Obviously, the mission can be endangered if a thruster fault occurs since it may have critical impact on the GNC system, i.e., it may lead to a degraded GNC performances or even the GNC become unstable. More precisely, we consider the following thruster fault scenarios:

- **Case 1: stuck open valve** - provides maximum thrust regardless of the demand;
- **Case 2: thruster closing itself (blocked-closed)** - thruster does not generate any thrust regardless of the demanded command by the TMF;
- **Case 3: bi-propellant leakage** - residual propellant leakage of size $m_{leak}(t)$, starting from 0 and reaching the maximum leakage size $\hat{m}_{leak} > 0$ with a given slope $m_s > 0$, i.e., $m_{leak}(t) = \min\{m_s(t - t_f), \hat{m}_{leak}\}$, where t_f denotes the time of fault occurrence;
- **Case 4: thrust loss** - loss of efficiency of a particular thruster by a value $\hat{m}_{loss} > 0$;

Assuming no simultaneous faults, the considered thruster fault scenarios can be modeled in a multiplicative way according to (index "f" is used to outline the faulty case)

$$\begin{pmatrix} \boldsymbol{F}_{thr}^{f}(t) \\ \boldsymbol{C}_{thr}^{f}(t) \end{pmatrix} = \boldsymbol{M}\left(\boldsymbol{I}_8 - \boldsymbol{\Psi}(t)\right)\boldsymbol{T}_{on}\left(t - \tau(t)\right) \tag{3}$$

with $\boldsymbol{\Psi}(t) = diag\big(\psi_1(t), \ldots, \psi_8(t)\big)$, where $0 \leq \psi_i(t) \leq 1$, $i = 1, ..., 8$ are unknown. The health status of the ith thruster is modeled by $\psi_i(t)$ as follows

$$\psi_i(t) = \begin{cases} 0 & \textbf{if healthy} \\ 1 - \varphi_i(t)/T_{on_i}(t) & \textbf{if faulty} \end{cases} \tag{4}$$

where $\varphi_i(t)$ allows to consider all four fault cases, mentioned earlier, as follows:

$$\varphi_i(t) = \begin{cases} \max\{T_{on_i}(t), m_{leak}(t)\} & \textbf{if case 1 or 3} \\ (1 - \hat{m}_{loss})T_{on_i}(t) & \textbf{if case 2 or 4} \end{cases} \tag{5}$$

where $0 < m_{leak}(t) < 1$ is the leakage size and $0 < \hat{m}_{loss} < 1$ is the efficiency loss size. It is obvious that $m_{leak}(t) = 1, \forall t$ models a fully open (stuck open valve) and $\hat{m}_{loss} = 1$ a blocked-closed thruster fault, respectively.

III. Modeling the Chaser Dynamics During the Rendezvous Phase

In this section, a linear position model and an attitude model of the chaser spacecraft dynamics are introduced for FDI purpose. The two proposed models are able to describe the dynamics of the chaser in both, fault-free and faulty situations. For the sake of brevity, we recall only the necessary developments about modeling the spacecraft's dynamics, available in the extensive space literature [33, 34].

A. Position Model

The translation motion of the chaser is derived from the 2nd Newton law. To proceed, let a, m, $\mathcal{G}$ and m_M denote the radius of the circular orbit of the target, the mass of the chaser during rendezvous, the universal gravitational constant and the mass of Mars. Then, the orbit of the rendezvous being circular, the velocity of the target is given by the relation

$$\sqrt{\frac{\mu}{a}} \tag{6}$$

where $\mu = \mathcal{G} \cdot m_M$. Let $\mathcal{R}_l = \{O_T; \vec{\boldsymbol{X}}_l, \vec{\boldsymbol{Y}}_l, \vec{\boldsymbol{Z}}_l\}$ be the local reference frame fixed at the center of target O_T, with its $\vec{\boldsymbol{Z}}_l$ axis be perpendicular to the $\vec{\boldsymbol{X}}_l$ and $\vec{\boldsymbol{Y}}_l$ axis and oriented as shown in Fig. 6.

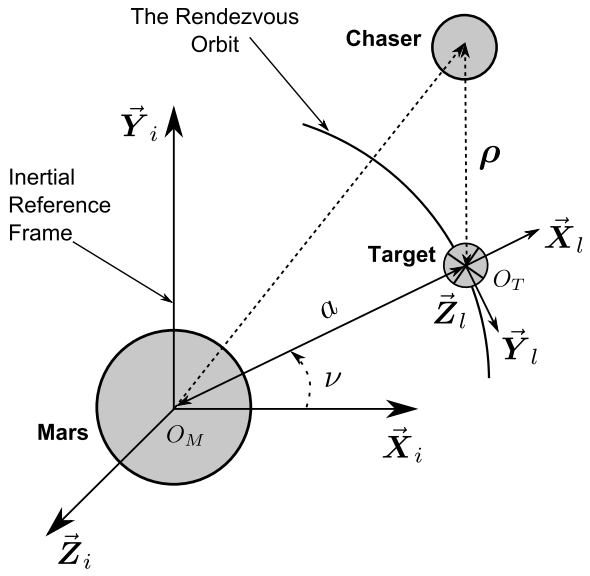

Fig. 6 The Mars rendezvous orbit with the associated frames.

The linear velocity of the target is given by the relation $a.n$, where $n = \dot{\nu}$ stands for the uniform angular speed of the target. This velocity is given in the inertial frame $\mathcal{R}_i = \{O_M; \vec{\boldsymbol{X}}_i, \vec{\boldsymbol{Y}}_i, \vec{\boldsymbol{Z}}_i\}$, which is attached to the center of Mars O_M. From the Kepler's third law it follows:

$$a.n = \sqrt{\frac{\mu}{a}} \Rightarrow n = \sqrt{\frac{\mu}{a^3}} \tag{7}$$

During the rendezvous phase, it is assumed that the chaser motion is due to the four following forces, all given in $\mathcal{R}_l$:

- the Mars attraction force $\boldsymbol{F}_a = -m\frac{\mu}{((a+\xi)^2+\eta^2+\zeta^2)^{3/2}}\big((a+\xi)\vec{\boldsymbol{X}}_l + \eta\vec{\boldsymbol{Y}}_l + \zeta\vec{\boldsymbol{Z}}_l\big)$, where ξ, η, ζ denote the elements of the three dimensional relative position vector $\boldsymbol{\rho} = [\xi, \eta, \zeta]^T$ of the chaser from the origin of the target frame O_T, expressed in $\mathcal{R}_l$;
- the centripetal force $\boldsymbol{F}_e = m\left(n^2(a+\xi)\vec{\boldsymbol{X}}_l + n^2\eta\vec{\boldsymbol{Y}}_l + 0\vec{\boldsymbol{Z}}_l\right)$;
- the Coriolis force $\boldsymbol{F}_c = m\left(2n\dot{\eta}\vec{\boldsymbol{X}}_l - 2n\dot{\xi}\vec{\boldsymbol{Y}}_l + 0\vec{\boldsymbol{Z}}_l\right)$;
- the non-gravitational (chemical thrust, perturbations) force $\boldsymbol{F}_d = F_{d\xi}\vec{\boldsymbol{X}}_l + F_{d\eta}\vec{\boldsymbol{Y}}_l + F_{d\zeta}\vec{\boldsymbol{Z}}_l$.

Then, from the 2nd Newton law, it follows

$$\begin{cases} \ddot{\xi} = n^2(a+\xi) + 2n\dot{\eta} - \frac{\mu}{\left((a+\xi)^2+\eta^2+\zeta^2\right)^{3/2}}(a+\xi) + \frac{F_{d\xi}}{m} \\ \ddot{\eta} = n^2\eta - 2n\dot{\xi} - \frac{\mu}{\left((a+\xi)^2+\eta^2+\zeta^2\right)^{3/2}}\eta + \frac{F_{d\eta}}{m} \\ \ddot{\zeta} = -\frac{\mu}{\left((a+\xi)^2+\eta^2+\zeta^2\right)^{3/2}}\zeta + \frac{F_{d\zeta}}{m} \end{cases} \tag{8}$$

Because the distance between the target and the chaser, during the rendezvous, is much smaller than the orbit, i.e., $\|\boldsymbol{\rho}\| \ll a$, it is possible to derive the so called Hill-Clohessy-Wiltshire (HCW) equations from Eq. (8) by means of a first order approximation [35]. Thus, the motion of the chaser can be modeled in the target (local) frame $\mathcal{R}_l$, in both fault free (i.e., $\Psi(t) = 0$) and faulty (i.e., $\Psi(t) \neq 0$) situations, according to a linear 6th order state space model with state vector $\boldsymbol{x} = [\xi\ \eta\ \zeta\ \dot{\xi}\ \dot{\eta}\ \dot{\zeta}]^T$, i.e., from Eq. (8) it follows

$$\begin{cases} \dot{\boldsymbol{x}}(t) = \boldsymbol{A}_p\boldsymbol{x}(t) + \boldsymbol{B}_p\boldsymbol{R}\big(\hat{Q}_{tgt}(t), \hat{Q}_{chs}(t)\big)\boldsymbol{F}^f_{thr}(t) + \boldsymbol{E}_{pw}\boldsymbol{w}(t) \\ \boldsymbol{y}(t) = \boldsymbol{C}_p\boldsymbol{x}(t) \end{cases} \tag{9}$$

where $\hat{Q}_{tgt} \in \mathbb{R}^4$ and $\hat{Q}_{chs} \in \mathbb{R}^4$ denote the attitude quaternion estimate of the target, and the chaser, respectively. The attitude estimate $\hat{Q}_{tgt}$ and $\hat{Q}_{chs}$ describe the orientation of the target body frame and the chaser body frame with respect to $\mathcal{R}_i$, respectively. These estimates are provided by the NAV unit. The quaternions dependent rotation matrix $\boldsymbol{R}(\cdot)$ performs the projection of the three-dimensional force vector $\boldsymbol{F}^f_{thr}$ from the chaser's frame on to the target frame $\mathcal{R}_l$. The measurement vector $\boldsymbol{y} = [\xi\ \eta\ \zeta]^T$ is expressed in $\mathcal{R}_l$ and measured by LIDAR. Spatial disturbances (solar radiation pressure, gravity gradient and atmospheric drag) are denoted by $\boldsymbol{w} \in \mathbb{R}^3$. $\boldsymbol{A}_p, \boldsymbol{B}_p, \boldsymbol{C}_p$ and $\boldsymbol{E}_{pw}$ are matrices of appropriate dimension.

Considering Eq. (2) and Eq. (3), a new input vector $\boldsymbol{u} \in \mathbb{R}^3$ is defined according to

$$\boldsymbol{u}(t) = \boldsymbol{R}\big(\hat{Q}_{tgt}(t), \hat{Q}_{chs}(t)\big)\boldsymbol{F}_{thr}(t) \tag{10}$$

and the fault model is approximated in terms of an additive fault vector $\boldsymbol{f} \in \mathbb{R}^3$ as follows:

$$\boldsymbol{f}(t) = -\boldsymbol{R}\big(\hat{Q}_{tgt}(t), \hat{Q}_{chs}(t)\big)\boldsymbol{M}_F\boldsymbol{\Psi}(t)\boldsymbol{T}_{on}\big(t - \tau(t)\big) \tag{11}$$

where $\boldsymbol{M}_F \in \mathbb{R}^{3\times 8}$ is the upper block of the thruster configuration matrix $\boldsymbol{M}^T = [\boldsymbol{M}_F^T\ \boldsymbol{M}_C^T]$, related to the forces $\boldsymbol{F}$, see Fig. 4 if necessary. This type of approximation is widely used in the literature [6, 36].

Finally, the overall model of the position dynamics that takes into account both, the attitude Q_{chs}, and the relative position $\boldsymbol{\rho}$, can be derived from Eq. (9) using Eqs. (10) and (11) as follows

$$\begin{cases} \dot{\boldsymbol{x}}(t) = \boldsymbol{A}_p \boldsymbol{x}(t) + \boldsymbol{B}_p \boldsymbol{u}(t) + \boldsymbol{E}_{pf} \boldsymbol{f}(t) + \boldsymbol{E}_{pw} \boldsymbol{w}(t) \\ \boldsymbol{y}(t) = \boldsymbol{C}_p \boldsymbol{x}(t) \end{cases} \tag{12}$$

where $\boldsymbol{E}_{pf} = \boldsymbol{B}_p$. This model is now suitable for the FDI filter design proposed in the next section.

B. Attitude Dynamics

The attitude control system works in a target pointing mode, which means that the chaser keeps one face of the spacecraft pointed to the target and maintains it during the whole rendezvous phase (see Fig 7 for illustration).

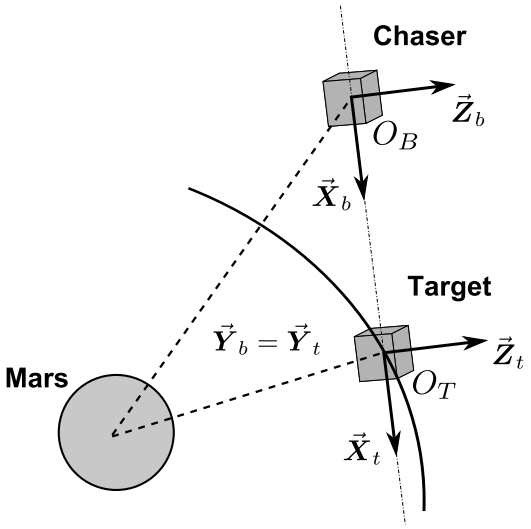

Fig. 7 Chaser target pointing.

The equations for the rotational motion of the chaser spacecraft in the body-fixed reference frame $\mathcal{R}_b = \{O_B; \vec{\boldsymbol{X}}_b, \vec{\boldsymbol{Y}}_b, \vec{\boldsymbol{Z}}_b\}$ (the center of this frame is fixed to the center of mass of the chaser) are derived from the Euler's equations of motion [37]

$$\dot{\boldsymbol{\omega}}(t) = \boldsymbol{I}_{chs}^{-1}\big(\boldsymbol{C}_{thr}(t) + \boldsymbol{C}_{dis}(t) - \boldsymbol{\omega}(t) \times \boldsymbol{I}_{chs}\boldsymbol{\omega}(t)\big) \tag{13}$$

where $\times$ denotes the cross product of vectors and $\boldsymbol{I}_{chs} \in \mathbb{R}^{3\times3}$ is the inertia matrix. $\boldsymbol{C}_{thr}$ and $\boldsymbol{C}_{dis}$ is the external torque about the center of mass due to the propulsion and disturbances, respectively. $\boldsymbol{\omega} = [p, q, r]^T$ is the chaser rotational velocity vector, expressed in body frame $\mathcal{R}_b$.

Using the individual rotation matrices from Euler(3,2,1) rotation we can express the relation between the rotational velocities $\boldsymbol{\omega}$ and the rate of the Euler angles $\boldsymbol{\Theta} = [\varphi, \theta, \psi]^T$. The inverse relationship becomes [33]

$$\dot{\boldsymbol{\Theta}}(t) = \frac{1}{\cos(\theta)} \begin{bmatrix} \cos(\theta) & \sin(\varphi)\sin(\theta) & \cos(\varphi)\sin(\theta) \\ 0 & \cos(\varphi)\cos(\theta) & -\sin(\varphi)\cos(\theta) \\ 0 & \sin(\varphi) & \cos(\varphi) \end{bmatrix} \boldsymbol{\omega}(t) \tag{14}$$

Finally, noting that the chaser is controlled around the equilibrium point $\boldsymbol{\Theta} = \mathbf{0}$ and $\boldsymbol{\omega} = \mathbf{0}$, one can derive from Eqs.(13-14) a linear model by means of a first-order approximation of the nonlinear equations around the equilibrium point. Let the system's state vector be $\boldsymbol{x} = [\varphi, \theta, \psi, p, q, r]^T$ and the measurement vector $\boldsymbol{y} = [\varphi, \theta, \psi]^T$, it boils down to a 6 order linear, pure attitude, model having the same structure as the position model given in Eq. (12), i.e.,

$$\begin{cases} \dot{\boldsymbol{x}}(t) = \boldsymbol{A}_a \boldsymbol{x}(t) + \boldsymbol{B}_a \boldsymbol{u}(t) + \boldsymbol{E}_{af} \boldsymbol{f}(t) + \boldsymbol{E}_{aw} \boldsymbol{w}(t) \\ \boldsymbol{y}(t) = \boldsymbol{C}_a \boldsymbol{x}(t) \end{cases} \tag{15}$$

where $\boldsymbol{w} \in \mathbb{R}^3$ denotes the spatial disturbances. The input $\boldsymbol{u}$ and the fault $\boldsymbol{f}$ vector are given by

$$\boldsymbol{u}(t) = \boldsymbol{C}_{thr}(t) \tag{16}$$

$$\boldsymbol{f}(t) = -\boldsymbol{M}_C \boldsymbol{\Psi}(t) \boldsymbol{T}_{on}\big(t - \tau(t)\big) \tag{17}$$

with $\boldsymbol{M}_C \in \mathbb{R}^{3\times 8}$ being the lower block of the thruster configuration matrix $\boldsymbol{M}$. The rest of the parameters $\boldsymbol{A}_a, \boldsymbol{B}_a, \boldsymbol{E}_{af}$ and $\boldsymbol{E}_{aw}$ are the result of the linearization procedure.

IV. Design of the FDI Scheme

This section is dedicated to the FDI task of thruster faults despite the presence of the delay $\tau(t)$ in the actuation system. Two fault diagnosis units based on the eigenstructure assignment (EA) approach of an observer-based fault detector are designed. The first is based on the position model (12) and the second one uses the attitude model (15). The isolation strategy is based on the evaluation of a cross-correlation like criterion between the component of the residuals and the thruster opening times.

A. Robust Residual Generator Design

Consider the following general description of the continuous LTI system

$$\begin{cases} \dot{\boldsymbol{x}}(t) = \boldsymbol{A}\boldsymbol{x}(t) + \boldsymbol{B}\boldsymbol{u}(t) + \boldsymbol{E}_f\boldsymbol{f}(t) \\ \boldsymbol{y}(t) = \boldsymbol{C}\boldsymbol{x}(t) \end{cases} \tag{18}$$

where $\boldsymbol{x} \in \mathbb{R}^{n_x}$, $\boldsymbol{u} \in \mathbb{R}^{n_u}$, $\boldsymbol{y} \in \mathbb{R}^{n_y}$, and $\boldsymbol{f} \in \mathbb{R}^{n_f}$ is state, input, measurement, and unknown fault vector, respectively. The quadruplet $\{\boldsymbol{A}, \boldsymbol{B}, \boldsymbol{C}, \boldsymbol{E}_f\}$ represents the state-space matrices either of the position Eq. (12), or the attitude Eq. (15) model. It is assumed that all considered faults $\boldsymbol{f}$ are detectable (see [38] for more details on fault delectability) and that the pair $(\boldsymbol{A}, \boldsymbol{C})$ is observable. The spatial disturbances $\boldsymbol{w}$ are omitted from Eq. (18), because they have the same directional properties as those of faults, i.e., $\boldsymbol{E}_f = \boldsymbol{E}_w$, and thus, exact spatial disturbance decoupling cannot be achieved.

The TMF generates the thrusters' opening times $\boldsymbol{T}_{on}$ equidistantly with a fixed sampling interval $T > 0$. The control signal $\boldsymbol{T}_{on}(k)$, generated at time $t = kT, k \in \mathbb{Z}^+$, arrives at the actuator at time instant $t = kT + \tau(k)$. Assuming that the time-varying delay $\tau(k)$ is unknown but upper bounded, i.e., $\tau(k) \leq \bar{\tau}, \forall k \in \mathbb{Z}^+$, then the system's input, affected by delays, is given by

$$\boldsymbol{u}(t) = \begin{cases} \boldsymbol{u}_c(k-1), & t \in \big[kT, kT + \tau(k)\big) \\ \boldsymbol{u}_c(k), & t \in \big[kT + \tau(k), (k+1)T\big) \end{cases} \tag{19}$$

where $\boldsymbol{u}_c$ depends on the selected model according to

$$\boldsymbol{u}_c(k) = \begin{cases} \boldsymbol{R}\big(\hat{Q}_{tgt}(k), \hat{Q}_{chs}(k)\big)\boldsymbol{M}_F\boldsymbol{T}_{on}(k), & \textbf{if } \text{position model is used} \\ \boldsymbol{M}_C\boldsymbol{T}_{on}(k), & \textbf{if } \text{attitude model is used} \end{cases} \tag{20}$$

Our objective is to design discrete-time residual generator $\boldsymbol{r}(z) = \boldsymbol{H}_y(z)\boldsymbol{y}(z) + \boldsymbol{H}_u(z)\boldsymbol{u}(z)$, so that $\boldsymbol{r}$ is robust against the uncertain delay $\tau(k)$, $\boldsymbol{H}_y$ & $\boldsymbol{H}_u$ being observer-based filter transfer functions. To achieve this goal, the influence of the uncertainty $\tau(k)$ is first transformed to unknown input acting on the system model and then decoupled by means of eigenstructure assignment technique.

To proceed, assume $\tau(k)$ can be expressed as: $\tau(k) = lT + \delta(k) \leq \bar{\tau}$, where l is a known integer, and $\delta(k) \in \mathbb{R}$ is the unknown varying part of $\tau(k)$, bounded by $0 \leq \delta(k) < mT$, with m being a

known integer. Following, assume $m = 1$, which means that the variation part of the delay is less than one sampling interval. The case when $m > 1$ is discussed in [39].

If we assume that $\boldsymbol{f}$ is constant during each sampling interval T, what is a reasonable assumption from a practical point of view (the counterpart of this assumption is that the sampling interval T is chosen adequately so that Eq. (21) holds), then the discrete representation of Eqs. (18) and (19) is

$$\begin{cases} \boldsymbol{x}(k+1) = \bar{\boldsymbol{A}}\boldsymbol{x}(k) + \boldsymbol{\Gamma}_0(\delta(k))\boldsymbol{u}_c(k-l) \\ \qquad\qquad + \boldsymbol{\Gamma}_1(\delta(k))\boldsymbol{u}_c(k-l-1) + \bar{\boldsymbol{E}}_f\boldsymbol{f}(k) \\ \boldsymbol{y}(k) = \bar{\boldsymbol{C}}\boldsymbol{x}(k) \end{cases} \tag{21}$$

where

$$\bar{\boldsymbol{A}} = e^{\boldsymbol{A}T},\ \boldsymbol{\Gamma}_0(\delta(k)) = \int_0^{T-\delta(k)} e^{\boldsymbol{A}t}dt\boldsymbol{B},\ \bar{\boldsymbol{E}}_f = \int_0^{T} e^{\boldsymbol{A}t}dt\boldsymbol{E}_f$$
$$\bar{\boldsymbol{C}} = \boldsymbol{C},\quad \boldsymbol{\Gamma}_1(\delta(k)) = \int_{T-\delta(k)}^{T} e^{\boldsymbol{A}t}dt\boldsymbol{B}$$

It's obvious that the following holds

$$\bar{\boldsymbol{B}} = \boldsymbol{\Gamma}_0(\delta(k)) + \boldsymbol{\Gamma}_1(\delta(k)) = \int_0^T e^{\boldsymbol{A}t}dt\boldsymbol{B} \tag{22}$$

Using (21) and (22), and introducing a new augmented state vector $\boldsymbol{z}^T(k) = [\ \boldsymbol{x}^T(k)\ \ \boldsymbol{u}_c^T(k-l-1)\ ]$, we obtain

$$\begin{cases} \boldsymbol{z}(k+1) = \left(\hat{\boldsymbol{A}}_0 + \hat{\boldsymbol{A}}(\delta(k))\right)\boldsymbol{z}(k) \\ \qquad\qquad + \left(\hat{\boldsymbol{B}}_0 + \hat{\boldsymbol{B}}(\delta(k))\right)\boldsymbol{u}_c(k-l) + \hat{\boldsymbol{E}}_f\boldsymbol{f}(k) \\ \boldsymbol{y}(k) = \hat{\boldsymbol{C}}\boldsymbol{z}(k) \end{cases} \tag{23}$$

where

$$\hat{\boldsymbol{A}}_0 = \begin{bmatrix} \bar{\boldsymbol{A}} & \boldsymbol{0} \\ \boldsymbol{0} & \boldsymbol{0} \end{bmatrix},\ \hat{\boldsymbol{A}}(\delta(k)) = \begin{bmatrix} \boldsymbol{0} & \boldsymbol{\Gamma}_1(\delta(k)) \\ \boldsymbol{0} & \boldsymbol{0} \end{bmatrix},\ \hat{\boldsymbol{C}} = \begin{bmatrix} \bar{\boldsymbol{C}} & \boldsymbol{0} \end{bmatrix}$$
$$\hat{\boldsymbol{B}}_0 = \begin{bmatrix} \bar{\boldsymbol{B}} \\ \boldsymbol{I} \end{bmatrix},\quad \hat{\boldsymbol{B}}(\delta(k)) = \begin{bmatrix} -\boldsymbol{\Gamma}_1(\delta(k)) \\ \boldsymbol{0} \end{bmatrix},\quad \hat{\boldsymbol{E}}_f = \begin{bmatrix} \bar{\boldsymbol{E}}_f \\ \boldsymbol{0} \end{bmatrix}$$

The system given in Eq. (23) is a time-varying system with unstructured uncertainty, where $\boldsymbol{\Gamma}_1(\delta(k))$ is strongly dependent on the uncertain term $\delta(k)$. The remaining task is to transform this model to an uncertain polytopic system for which structured properties can be extracted in terms of unknown

inputs. The polytopic system is then rewritten as a LTI system subject to an unknown input with a suitable distribution matrix.

Two polytopic transformations are used for this purpose. The first uses a Cayley-Hamilton theorem based transformation [39] and is introduced in Proposition 1.

Proposition 1. The Cayley-Hamilton theorem based transformation of $\mathbf{\Gamma}_1(\delta(k))$ can be expressed as the convex matrix polytope

$$\mathbf{\Gamma}_1^a(\delta(k)) = \sum_{i=1}^{2n_x} \mu_i^a(k) \boldsymbol{U}_i^a \tag{24}$$

where $\mu_i^a(k) > 0, i = 1, ..., 2n_x, \forall k \in \mathbb{Z}^+$ are uncertain scale factors satisfying $\sum_{i=1}^{2n_x} \mu_i^a(k) = 1, \forall k \in \mathbb{Z}^+$, and $\boldsymbol{U}_i^a, i = 1, \ldots, 2n_x$ are known constant matrices given in Appendix A.

The second transformation is based on the h-order Taylor series expansion [40] and is given in Proposition 2.

Proposition 2. The h-order Taylor series approximation of $\mathbf{\Gamma}_1(\delta(k))$ can be expressed as the convex matrix polytope

$$\mathbf{\Gamma}_1^b(\delta(k)) = \sum_{i=1}^{h+1} \mu_i^b(k) \boldsymbol{U}_i^b \tag{25}$$

where $\mu_i^b(k) > 0, i = 1, ..., h+1, \forall k \in \mathbb{Z}^+$ are uncertain scale factors satisfying $\sum_{i=1}^{h+1} \mu_i^b(k) = 1, \forall k \in \mathbb{Z}^+$, and $\boldsymbol{U}_i^b, i = 1, \ldots, h+1$ are known constant matrices given in Appendix B.

Taking into account the structure of the uncertain matrices $\hat{\boldsymbol{A}}(\delta)$ and $\hat{\boldsymbol{B}}(\delta)$ in Eq. (23) and the two transformations of $\mathbf{\Gamma}_1(\delta)$ introduced in Eq. (24) and Eq. (25), the influence of the uncertain scalar factors μ_i^a and μ_i^b on the state $\boldsymbol{x}$ can be approximated in terms of unknown inputs as

$$\sum_{i=1}^{2n_x} \mu_i^a(k) \boldsymbol{U}_i^a \Big(\boldsymbol{u}_c(k-l-1) - \boldsymbol{u}_c(k-l) \Big) = \boldsymbol{E}_d^a \boldsymbol{d}_a(k) \tag{26}$$

$$\sum_{i=1}^{h+1} \mu_i^b(k) \boldsymbol{U}_i^b \Big(\boldsymbol{u}_c(k-l-1) - \boldsymbol{u}_c(k-l) \Big) = \boldsymbol{E}_d^b \boldsymbol{d}_b(k) \tag{27}$$

where

$$\boldsymbol{d}_a(k) = \left[\mu_1^a(k) \big(\boldsymbol{u}_c^T(k-l-1) - \boldsymbol{u}_c^T(k-l) \big), ..., \mu_{2n_x}^a(k) \big(\boldsymbol{u}_c^T(k-l-1) - \boldsymbol{u}_c^T(k-l) \big) \right]^T$$

$$\boldsymbol{d}_b(k) = \left[\mu_1^b(k) \big(\boldsymbol{u}_c^T(k-l-1) - \boldsymbol{u}_c^T(k-l) \big), ..., \mu_{h+1}^b(k) \big(\boldsymbol{u}_c^T(k-l-1) - \boldsymbol{u}_c^T(k-l) \big) \right]^T$$

$$\boldsymbol{E}_d^a = \left[\boldsymbol{U}_1^a, ..., \boldsymbol{U}_{2n_x}^a \right], \quad \boldsymbol{E}_d^b = \left[\boldsymbol{U}_1^b, ..., \boldsymbol{U}_{h+1}^b \right]$$

Now, the mean value of the two unknown inputs, $\boldsymbol{d}_a$ and $\boldsymbol{d}_b$, is considered. The augmented distribution matrix $\hat{\boldsymbol{E}}_d$ and the augmented unknown input $\boldsymbol{d}$ take the following forms

$$\hat{\boldsymbol{E}}_d = \begin{bmatrix} \bar{\boldsymbol{E}}_d \\ \mathbf{0} \end{bmatrix} = \begin{bmatrix} \boldsymbol{E}_d^a & \boldsymbol{E}_d^b \\ \mathbf{0} \end{bmatrix}, \ \boldsymbol{d}(k) = \tfrac{1}{2} \begin{bmatrix} \boldsymbol{d}_a(k) \\ \boldsymbol{d}_b(k) \end{bmatrix} \tag{28}$$

The elements (columns) $\hat{\boldsymbol{E}}_d$ define the directions how each component of $\boldsymbol{d}$ affects the augmented state. This kind of approach gains advantage of combining two techniques to model the effect of the complex uncertainty δ on the state.

Finally, the augmented model with lumped unknown inputs can be expressed as

$$\begin{cases} \boldsymbol{z}(k+1) = \hat{\boldsymbol{A}}_0 \boldsymbol{z}_k + \hat{\boldsymbol{B}}_0 \boldsymbol{u}_c(k-l) + \hat{\boldsymbol{E}}_f \boldsymbol{f}(k) + \hat{\boldsymbol{E}}_d \boldsymbol{d}(k) \\ \boldsymbol{y}(k) = \hat{\boldsymbol{C}} \boldsymbol{z}(k) \end{cases} \tag{29}$$

This model is a quasi-equivalent representation of the augmented system given in Eq. (23), in other words, using two polytopic transformations, the influence of the uncertainty $\boldsymbol{\Gamma}_1(\delta)$ on the augmented state $\boldsymbol{z}$ is approximated in terms of unknown input $\boldsymbol{d}$.

By closer examining the structure of $\hat{\boldsymbol{A}}_0, \hat{\boldsymbol{B}}_0, \hat{\boldsymbol{E}}_f, \hat{\boldsymbol{E}}_d$ in Eq. (29), one can see that only the upper state of $\boldsymbol{z}$, i.e., the system state $\boldsymbol{x}$, is influenced by $\boldsymbol{f}$ and $\boldsymbol{d}$ and, that there is no coupling between the lower and upper state. This allows us to consider only the upper state $\boldsymbol{x}$ in Eq. (29) for residual generator design. The following observer-based residual generator with matrices $\bar{\boldsymbol{A}}, \bar{\boldsymbol{B}}, \bar{\boldsymbol{C}}, \bar{\boldsymbol{E}}_f$, and $\bar{\boldsymbol{E}}_d$ is thus considered:

$$\begin{cases} \hat{\boldsymbol{x}}(k+1) = (\bar{\boldsymbol{A}} - \boldsymbol{L}\bar{\boldsymbol{C}})\hat{\boldsymbol{x}}(k) + \bar{\boldsymbol{B}} \boldsymbol{u}_c(k-l) + \boldsymbol{L}\boldsymbol{y}(k) \\ \boldsymbol{r}(k) = \boldsymbol{Q}\big(\boldsymbol{y}(k) - \bar{\boldsymbol{C}}\hat{\boldsymbol{x}}(k)\big) \end{cases} \tag{30}$$

where $\boldsymbol{r} \in \mathbb{R}^{n_r}$, $\hat{\boldsymbol{x}} \in \mathbb{R}^{n_x}$ is the residual, and the state estimation vector, respectively. The matrix $\boldsymbol{Q} \in \mathbb{R}^{n_r \times n_y}$ is the residual weighting matrix.

The Z-transformed residual response to faults and unknown inputs is

$$\boldsymbol{r}(z) = \boldsymbol{G}_{rf}(z)\boldsymbol{f}(z) + \boldsymbol{G}_{rd}(z)\boldsymbol{d}(z) \tag{31}$$

where $\boldsymbol{G}_{rf}(z)$ and $\boldsymbol{G}_{rd}(z)$ denote the transfers between $\boldsymbol{f}(z)$ and $\boldsymbol{r}(z)$, and $\boldsymbol{d}(z)$ and $\boldsymbol{r}(z)$, respectively. Once $\bar{\boldsymbol{E}}_d$ is known, the remaining problem is to find matrices $\boldsymbol{L}$ and $\boldsymbol{Q}$ so that $(\bar{\boldsymbol{A}} - \boldsymbol{L}\bar{\boldsymbol{C}})$ is stable, and $\boldsymbol{G}_{rd}(z) = \mathbf{0}$ holds. The assignment of the observer eigenvectors and eigenvalues is

a direct way to solve this design problem. Note that, because this technique does not consider a sensitivity constraint in the design procedure, therefore the fault sensitivity performance of the proposed FDI scheme can only be verified a posteriori. Especially, the subspace of considered faults should not intersect the subspace of decoupled disturbances [41], i.e., $\mathrm{Im}(\bar{\boldsymbol{E}}_f) \not\subset \mathrm{Im}(\bar{\boldsymbol{E}}_d)$.

The following lemmas and theorems give the solution to the design problem.

Lemma 1. The transfer function $\boldsymbol{G}_{rd}(z)$ can be expanded in terms of the eigenstructure as

$$\boldsymbol{G}_{rd}(z) = \boldsymbol{H}(z\boldsymbol{I} - \bar{\boldsymbol{A}}_c)^{-1}\bar{\boldsymbol{E}}_d = \sum_{i=1}^{n_x} \frac{\boldsymbol{H}\boldsymbol{v}_i \boldsymbol{l}_i^T \bar{\boldsymbol{E}}_d}{z - \lambda_i} \tag{32}$$

where $\boldsymbol{H} = \boldsymbol{Q}\bar{\boldsymbol{C}}$, $\boldsymbol{v}_i$ and $\boldsymbol{l}_i^T$ are the right and left eigenvectors of $\bar{\boldsymbol{A}}_c = \bar{\boldsymbol{A}} - \boldsymbol{L}\bar{\boldsymbol{C}}$ associated with eigenvalue λ_i.

Lemma 2. A given left eigenvector $\boldsymbol{l}_i^T$ of $\bar{\boldsymbol{A}}_c$ is always orthogonal to the right eigenvectors $\boldsymbol{v}_j$ corresponding to the remaining $(n_x - 1)$ eigenvalues λ_j of $\bar{\boldsymbol{A}}_c$, where $\lambda_i \neq \lambda_j$.

Theorem 1 (Unknown input decoupling using left EA). If the necessary condition

$$\boldsymbol{Q}\bar{\boldsymbol{C}}\bar{\boldsymbol{E}}_d = \boldsymbol{H}\bar{\boldsymbol{E}}_d = \boldsymbol{0} \tag{33}$$

holds and all rows of the matrix $\boldsymbol{H}$ are left eigenvectors of $\bar{\boldsymbol{A}}_c$ corresponding to n_r eigenvalues of $\bar{\boldsymbol{A}}_c$, then $\boldsymbol{G}_{rd}(z) = \boldsymbol{0}$ is satisfied. The proof of this theorem can be found in [42].

Following the above lemmas and theorem the first step for the design of the unknown input decoupled residual generator (30) is to compute the weighting matrix $\boldsymbol{Q}$ such that it satisfies Eq. (33). The maximum row rank of $\boldsymbol{Q}$ is $n_y - \mathrm{rank}(\bar{\boldsymbol{C}}\bar{\boldsymbol{E}}_d)$, thus the residual signal dimension should be chosen according to

$$n_r \leq n_y - \mathrm{rank}(\bar{\boldsymbol{C}}\bar{\boldsymbol{E}}_d) \tag{34}$$

The second step is to determine the eigenstructure of the observer. All rows of $\boldsymbol{H}$ must be the n_r left eigenvectors of $\bar{\boldsymbol{A}}_c$. The remaining $n - n_r$ left eigenvectors can be chosen without restraint. For the given (stable) eigenvalue spectrum $\Lambda(\bar{\boldsymbol{A}}_c) = \{\lambda_i, i = 1, \ldots, n_x\}$, the following relation holds

$$\boldsymbol{l}_i^T(\lambda_i\boldsymbol{I} - \bar{\boldsymbol{A}}) = -\boldsymbol{l}_i^T\boldsymbol{L}\bar{\boldsymbol{C}} = -\boldsymbol{m}_i^T\bar{\boldsymbol{C}}, \quad i = 1, \ldots, n_x \tag{35}$$

where $\boldsymbol{m}_i^T = \boldsymbol{l}_i^T\boldsymbol{L}$. The assignability condition says that for each λ_i, the corresponding left eigenvector $\boldsymbol{l}_i^T$ should lie in the column subspace spanned by $\{\bar{\boldsymbol{C}}(\lambda_i\boldsymbol{I} - \bar{\boldsymbol{A}})^{-1}\}$, i.e., a vector $\boldsymbol{m}_i^T$ exists

such that

$$\boldsymbol{l}_i^T = \boldsymbol{m}_i^T \boldsymbol{K}_i, \qquad i = 1, \ldots, n_r \tag{36}$$

where $\boldsymbol{K}_i = -\bar{\boldsymbol{C}}(\lambda_i \boldsymbol{I} - \bar{\boldsymbol{A}})^{-1}$, $i = 1, \ldots, n_r$. The projection of $\boldsymbol{l}_i$ in the subspace span$\{\boldsymbol{K}_i\}$ is denoted by

$$\boldsymbol{l}_i^{\circ T} = \boldsymbol{m}_i^{\circ T} \boldsymbol{K}_i, \qquad i = 1, \ldots, n_r \tag{37}$$

where $\boldsymbol{m}_i^{\circ T} = \boldsymbol{l}_i^T \boldsymbol{K}_i^T (\boldsymbol{K}_i \boldsymbol{K}_i^T)^{-1}$, $i = 1, \ldots, n_r$.

If $\boldsymbol{l}_i^T = \boldsymbol{l}_i^{\circ T}$, $\boldsymbol{l}_i^T$ is in span$\{\boldsymbol{K}_i\}$, the required observer eigenstructure is assignable and perfect decoupling can be achieved. Otherwise, the eigenvectors must be chosen to be close, e.g., in a least-square sense $\|\boldsymbol{l}_i^T - \boldsymbol{l}_i^{\circ T}\|$, to the desired eigenvectors, i.e., an approximative procedure must be considered in order to replace $\boldsymbol{l}_i^T$ by its projection $\boldsymbol{l}_i^{\circ T}$. In this situation, the residuals have low sensitivity to unknown inputs due to approximate decoupling [22].

The remaining $n_x - n_r$ eigenvalues and corresponding eigenvectors can be chosen freely from the assignable subspace, e.g., using singular value decomposition (SVD). Then, the observer matrix $\boldsymbol{L}$ can be computed as follows

$$\boldsymbol{L} = \boldsymbol{P}^{-1} \boldsymbol{S} \tag{38}$$

where

$$\boldsymbol{S} = \begin{bmatrix} \boldsymbol{m}_1^\circ & \ldots & \boldsymbol{m}_{n_r}^\circ & \boldsymbol{m}_{n_r+1} & \ldots & \boldsymbol{m}_{n_x} \end{bmatrix}^T$$
$$\boldsymbol{P} = \begin{bmatrix} \boldsymbol{l}_1^\circ & \ldots & \boldsymbol{l}_{n_r}^\circ & \boldsymbol{l}_{n_r+1} & \ldots & \boldsymbol{l}_{n_x} \end{bmatrix}^T$$

It is obvious, that the first n_r eigenvalues corresponding to the required eigenvectors $\boldsymbol{l}_i^T, i = 1, \ldots, n_r$ must be real because all these eigenvectors are real-valued.

Remark 1. Without loss of generality, it can be assumed that $\bar{\boldsymbol{E}}_d$ has a full column rank. When this is not the case, the following decomposition can be applied: $\bar{\boldsymbol{E}}_d \boldsymbol{d}(k) = \bar{\boldsymbol{E}}_{d1} \bar{\boldsymbol{E}}_{d2} \boldsymbol{d}(k)$, where $\bar{\boldsymbol{E}}_{d1}$ is a full column rank matrix and $\bar{\boldsymbol{E}}_{d2} \boldsymbol{d}(k)$ can now be considered as a new unknown input.

1. Computational Results

First, the position model (Eq. (12)) and the attitude model (Eq. (15)) are transformed into the discrete form (21) with $l = 0$ and $m = 1$. It practically means, that the unknown time-varying delay

$\tau(k)$ is assumed to be in the closed interval $[0, T)$. Using the Cayley-Hamilton theorem given in proposition 1 and the 2nd order ($h = 2$) Taylor series expansion given in proposition 2, the uncertain time-varying delay $\tau(k)$ is modeled as an unknown input as in Eq. (28).

The resulting $\bar{\boldsymbol{E}}_d$ matrix has a large number of columns and the rank condition given by Eq. (34) cannot be explicitly satisfied. Choosing the desired residual dimension be equal to one, i.e., $n_r = 1$, the following low rank factorization is performed for both models:

$$\bar{\boldsymbol{E}}_d^* = \arg\min \|\bar{\boldsymbol{E}}_d - \bar{\boldsymbol{E}}_d^*\|_F^2, \quad \text{s.t.} \quad n_r = n_y - \text{rank}(\bar{\boldsymbol{C}}\bar{\boldsymbol{E}}_d^*) \tag{39}$$

By this factorization, the most significant directions are kept. Finally, a full column rank decomposition is performed on $\bar{\boldsymbol{E}}_d^*$ using SVD decomposition.

The obtained distribution matrix is used for the residual generator design given by Eq. (30). The desired left eigenvectors of the observer are the rows of the matrix $\boldsymbol{H} = \boldsymbol{Q}\bar{\boldsymbol{C}}$ where the weighting matrix $\boldsymbol{Q}$ is determined such that Eq. (33) is satisfied. In order to compare the FDI performances of both (position and attitude) models, the assigned eigenvalues (dynamics of the observer) were selected to be exactly the same for both models, i.e., $\Lambda(\bar{\boldsymbol{A}}_c) = \{0.85, 0.87, 0.89, 0.91, 0.93, 0.95\}$.

2. Comments on Implementation Issues

In order to avoid using an optimization procedure to determine s_i^{max} and s_i^{min} in Eq. (49), the solutions $s_i(t), i = 1, \ldots, n_x$ of the differential equation (48) were found numerically, and therefore, s_i^{max} and s_i^{min} can be found using a simple iterative method. It is worth noting that other exact unknown input (disturbance) decoupling methods exist [42]. In our particular case only the left EA technique appeared to be a viable candidate. Other methods, such as UIO or right EA technique, violated some necessary conditions of the solution existence.

B. Residual Evaluation and Fault Isolation

Once the residual generation problem is solved, the problem is to make a decision about the fault presence. The generalized likelihood ratio (GLR) test is used here [43]. The decision is made based on two hypotheses: H_0, the null hypothesis means no fault is present, while H_1, the alternative hypothesis, indicates some anomaly in the system considered to be due to the thruster fault. In this

case, the decision test $\varrho^{J_{th}}$ is defined by

$$\varrho^{J_{th}} = \begin{cases} S^{N_d}(k) \leq J_{th},\ H_0 \ \text{ is accepted} \\ S^{N_d}(k) > J_{th},\ H_1 \ \text{ is accepted} \end{cases} \tag{40}$$

where J_{th} is a fixed threshold selected by the designer and $S^{N_d}(k)$ is given by

$$S^{N_d}(k) = N_d \ln(\sigma_0) - \frac{N_d}{2}\left(1 + \ln(\hat{\sigma}_1^2(k)) - \frac{\hat{\sigma}_1^2(k)}{\sigma_0^2}\right), \qquad \hat{\sigma}_1^2(k) = \frac{1}{N_d}\sum_{j=k-N_d+1}^{k} r^2(j) \tag{41}$$

where r is the residual signal, σ_0 is the standard deviation of r in fault free situation, and $N_d > 1$ represents the detection sliding window due to on-line realization aspects. The interested reader can refer to the monograph of Basseville and Nikiforov [44] for details on the threshold determination.

In this paper, a cross-correlation test between the residual r and the associated thruster open duration T_{on_i} is considered for fault isolation purposes. In the thruster configuration of Fig. 3, each thruster has its partner which provides same torque but force in exactly opposite direction. Therefore, a full coverage of the isolation problem cannot be solved based on the so-called "sub-space isolation approach" because this test cannot distinguish between faults in either thruster, only in the thruster pair [38]. Structured observer schemes could be possible candidates for thruster fault isolation [45]. They are based on making each residual signal sensitive to a subset of faults while being insensitive to another subset. This, however, requires a bank of observers to be designed and run in parallel. Due to the on-board computational limitations, the following considers an alternative solution that requires only one observer.

The proposed isolation strategy is based on minimum $\underline{\sigma}^N$ or maximum $\bar{\sigma}^N$ cross-correlation criterion between the residual signal r and T_{on_i}, i.e.,

$$\sigma^N(k) = \begin{cases} \underline{\sigma}^N(k) & \textbf{if fault case 1 or 3} \\ \bar{\sigma}^N(k) & \textbf{if fault case 2 or 4} \end{cases} \tag{42}$$

where

$$\bar{\sigma}^N(k) = \arg\max_i \left| \frac{1}{N+1} \sum_{j=k-N+1}^{k} r(j) T_{on_i}(j) \right|, \ \ i = 1...8, \ \ \forall k \in \mathbb{Z}^+ \tag{43}$$

$$\underline{\sigma}^N(k) = \arg\min_i \left| \frac{1}{N + \Omega_i^N(k)} \sum_{j=k-N+1}^{k} r(j) T_{on_i}(j) \right|, \ \ i = 1...8, \ \ \forall k \in \mathbb{Z}^+ \tag{44}$$

$$\Omega_i^N(k) = 1 - \sum_{j=k-N+1}^{k} \varphi_i(j), \;\; i = 1, \ldots, 8, \quad \varphi_i(j) = \begin{cases} 0 & \textbf{if} \quad T_{on_i}(j) \neq 0 \\ 1 & \textbf{if} \quad T_{on_i}(j) = 0 \end{cases}$$

These cross-correlation functions are statistical quantities that try to find the associated thruster index that has the smallest/greatest impact on the resulting residual signal. For real-time reason, these criteria are computed on a N-length sliding-window. An increase in the value of N results in elongated isolation time delay. Hence again, an optimal value of N has to be selected. The resulting index $\sigma^N(k) \in \{1, 2, \ldots, 8\}$ refers to the identified faulty thruster at time instance k.

Finally, the resulting thruster index is confirmed at time instant k, if the following holds:

$$\sigma^N(k) = \sigma^N(k-1) = \ldots = \sigma^N(k - N_c + 1) \tag{45}$$

where a confirmation window of length $N_c > 1$ is introduced in order to avoid initial transition phenomena and to ensure robustness.

A key feature of this isolation strategy is that it is static, and thus, it has a low computational burden. Note that if the ith thruster is not used by the TMF, i.e., $T_{on_i} = 0$, the minimum cross-correlation function will possibly result in $\underline{\sigma}(k) = i$. This fact is taken into account by introducing a penalty function $\Omega_i^N(k)$ in (44).

Remark 2. It should be noted that an event resolution algorithm must be implemented for the decision given by Eq. (42), since it is required to distinguish the fault cases 1-3 from the case 2-4. Fortunately, because cases 1-3 imply a propellant overconsumption and since the chaser is equipped with a dedicated sensor that monitors the overall propellant consumption, this problem can be easily solved.

C. Computational Procedure

In order to ensure robustness, whilst being sensitive to faults, the threshold J_{th} has to be selected carefully. A higher value of J_{th} will increase the non-detection rate while a lower threshold will increase the false alarm rate. The optimal value of J_{th} can be selected through Monte Carlo (MC) simulation. This approach is widely used in the FDI community to analyze the efficiency and performance of the designed algorithm [11]. Here a set of 200 fault free MC simulations were

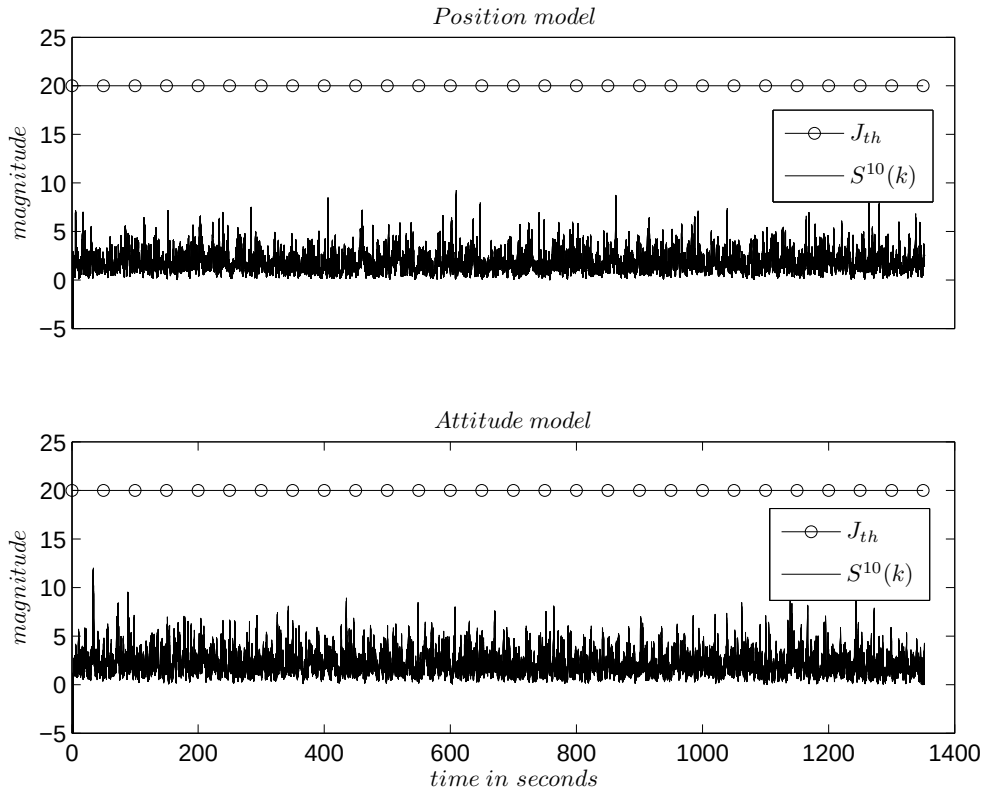

Fig. 8 A set of 200 Monte Carlo simulations for fault-free case.

performed using $N_d = 10$ in Eq. 41, i.e., the notation S^{10} is used. It can be clearly seen from Fig. 8, that for both models signal $S^{10}(k)$ does not exceed 20 in all the cases. Therefore, for the simulations in the next section, threshold of $J_{th} = 20$ is chosen to ensure (ideally) a zero false alarm rate. For the isolation function $\sigma^N(k)$, a sliding window of $N = 10$ and confirmation window of $N_c = 15$ samples was considered.

V. Simulation Results

The two FDI schemes described in the previous section are next implemented within the MSR "high-fidelity" industrial simulator, provided by Thales Alenia Space. All simulations are carried out under realistic conditions, i.e., the NAV unit is not considered to deliver "perfect" state estimates. We also assume constant time delay between the NAV and the control block, time-varying delays induced by the electronic devices, spatial disturbances (e.g., solar radiation pressure, gravity gradient, atmospheric drag) and parameter uncertainties. The simulations are all carried out during the last 20m of the rendezvous phase.

A set of $n_{mc} = 1600$ Monte Carlo simulations, for each faulty case ($4 \times n_{mc}$), have been run in order to assess the performances of the two proposed FDI schemes. For each run, model parameters, e.g., mass, center of mass (CoM), etc., were altered within a specific limit, see Table 1 for details. The mass, CoM and inertia were scattered according to the normal distribution and truncated to the corresponding 3σ value. Uncertainties of thruster rise times and thruster misalignment phenomena are modeled by 1% uncertainty on thruster forces.

Table 1 Parameter uncertainties of the chaser spacecraft (3 sigma)

Parameter	Variation range	Unit
Mass	$\pm 10\%$	$[kg]$
Inertia	$\pm 20\%$	$[kg.m^2]$
Thrusters forces	$\pm 1\%$	$[N]$
CoM	± 3	$[cm]$

Thruster faults were uniformly distributed among all of the 8 thrusters. Correspondingly, the leakage and the thrust loss size were drawn from the uniform distribution with the following range: $\hat{m}_{leak} \in < 10\%, 30\% >$ and $\hat{m}_{loss} \in < 40\%, 90\% >$. The leakage is implemented as a dynamic lower saturation to the commanded thruster open rate, where this saturation starts at value 0 and ends at $\hat{m}_{leak}$ with a slope of $m_s = 0.1$. In all cases, fault occurs at time $1000s$ and is maintained.

Figures 9 and 10 illustrate the behaviour of the most important characteristics of the FDI units and their internal signals. Both the position model-based (left figures on Fig. 9 and 10) and attitude model-based (right figures on Fig. 9 and 10) FDI units are considered. These characteristics are:

i) the GLR signal $S^{10}(k)$ represented at each sample k and for a detection sliding window of length $N_d = 10$ samples, see Eq. (41);

ii) the decision (alarm) signal $\varrho^{20}(k)$ with the defined threshold $J_{th} = 20$, see Eq. (40);

iii) the thruster declared to be faulty by an isolation unit which is represented by the signal $\sigma^{10}(k)$ for a computation sliding window of length $N = 10$ samples, see Eqs. (42)-(44).

The confirmation time window of length $N_c = 15$ samples is also considered. Figures 9 and 10 also illustrate from top to bottom, the above listed characteristics for the following set of four arbitrary

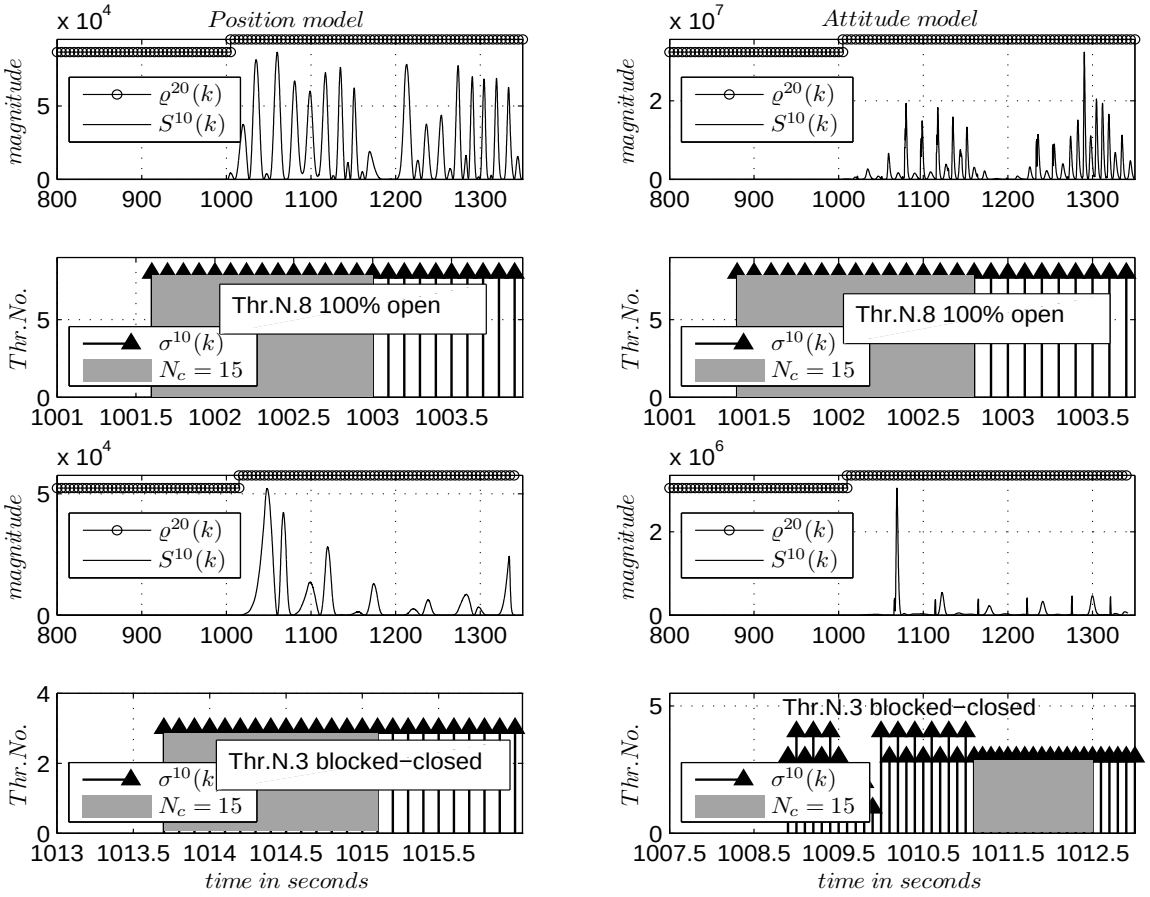

Fig. 9 Behaviour of the internal signals of the position (on the left) and attitude (on the right) model-based FDI scheme, respectively.

chosen faulty situations selected from the scattered parameter space listed in Table 1:

- A fault that corresponds to a stuck open valve, occurs in the thruster No.8., i.e., the thruster No. 8 is fully opened so that it provides a maximum thrust;
- A fully blocked-closed fault occurs in thruster No.3. In this case, the thruster does not generate any thrust regardless of the command by the TMF;
- The third faulty situation corresponds to thruster No.2 suffering from a leakage of size 19.2%;
- The fourth faulty situation corresponds to the case when the thruster No.7 loses its thrust level by a value of 54.7%.

Figure 9 is concerned with the two first situations whereas Fig. 10 considers the two last cases.

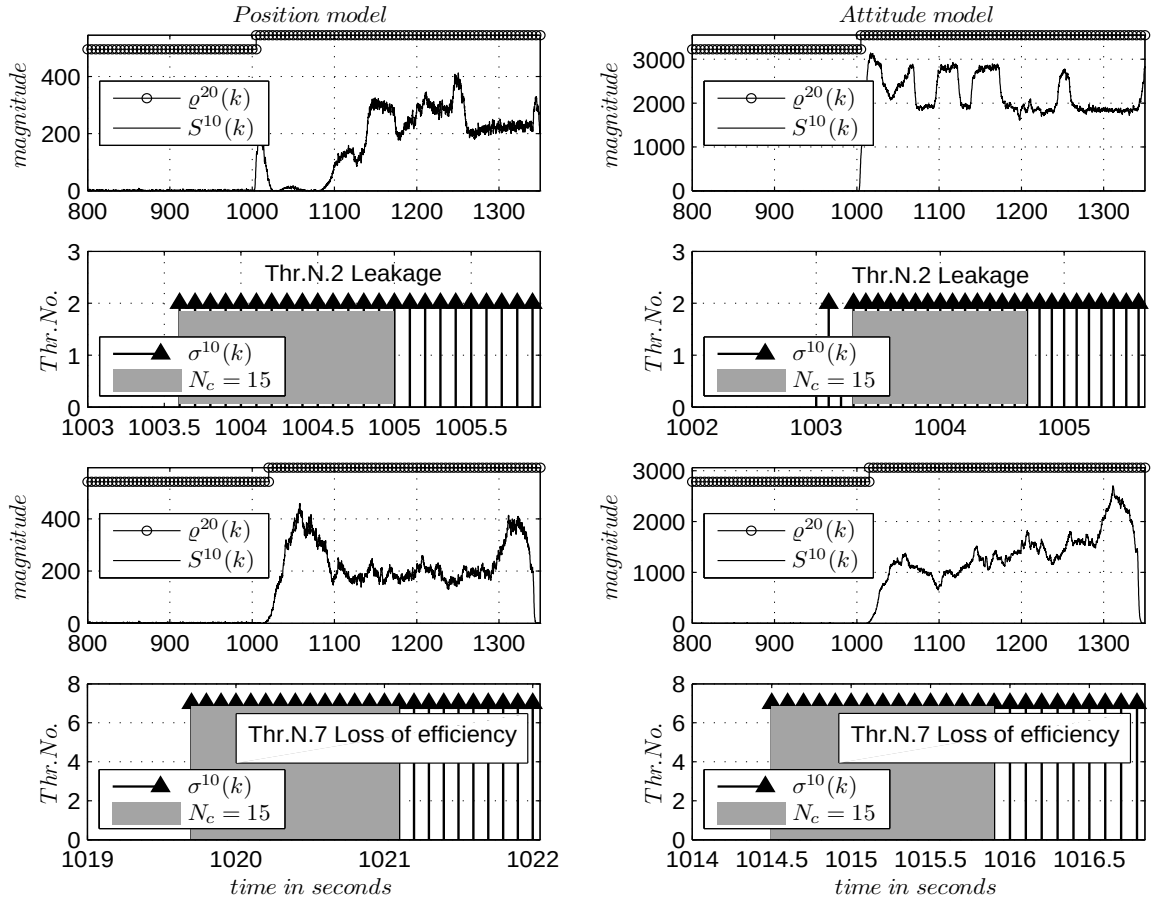

Fig. 10 Behaviour of the internal signals of the position (on the left) and attitude (on the right) model-based FDI scheme, respectively.

Clearly, the nonlinear simulations show that faults are detected and isolated by the proposed FDI units within a reasonable time. Moreover, Fig. 10 shows the ability to detect and isolate small (thrust loss) and incipient (residual leakage) thruster faults.

To evaluate the performance and reliability of the two FDI schemes, some statistical indices have been used, i.e., the detection time t_d (time from fault occurrence to fault detection) and isolation time t_i (time from fault occurrence to fault isolation) are computed. The considered indices are listed below.

- $mean(t_d)/mean(t_i)$ - mean detection/isolation time in seconds;
- $std(t_d)/std(t_i)$ - standard deviation of the detection/isolation time in seconds;
- *nondetection rate* P_{nd} - number of non-detections divided by n_{mc};

- *false alarm rate* P_f - number of wrongly detected faults divided by n_{mc}; and
- *true isolation rate* P_i - number of correctly isolated thrusters divided by n_{mc}.

These performance indices are calculated for each fault scenario and model separately.

Table 2 FDI performances based on 4x1600 Monte Carlo runs

	FDI based on position model				**FDI based on attitude model**			
Criterion	**CASE 1**	**CASE 2**	**CASE 3**	**CASE 4**	**CASE 1**	**CASE 2**	**CASE 3**	**CASE 4**
$mean(t_d)$	1.6	16.3	3.6	18.8	1.4	11.7	2.9	12.2
$std(t_d)$	0.017	3.803	0.167	6.594	0.048	2.895	0.076	3.064
$mean(t_i)$	3.4	17.9	5.5	20.4	3.6	15.0	5.5	15.6
$std(t_i)$	0.207	3.799	0.399	6.592	0.237	3.231	0.459	3.456
$P_{nd}/P_f/P_i$	0/0/1	0/0/1	0/0/1	0/0/1	0/0/1	0/0/1	0/0/1	0/0/1

Table 2 presents complete results obtained from the Monte Carlo simulation campaign. As it can be seen from this table, the two proposed FDI schemes present good reliability characteristics since no false alarms $P_f = 0$ and non-detections $P_{nd} = 0$ have been revealed. Furthermore, all thruster faults were correctly isolated at the end of the campaign, i.e., $P_i = 1$. These achieved results also demonstrate that each FDI scheme is able to successfully detect and isolate the chaser thruster faults.

In order to better appreciate the results presented in Table 2, a histogram plot is performed to graphically represent the distribution of the detection t_d and isolation t_i times, respectively. Figure 11 shows a comparison of the obtained results in terms of detection times and Fig. 12 in terms of isolation times. This visual representation allows to evaluate the FDI performances in terms of minimum and maximum detection/isolation times, as well as to observe the median values.

It can be seen from Fig. 11, that (as expected) the FDI unit based on the attitude model presents a greater sensitivity towards all faulty situations. This can be easily explained by the fact that attitude is more sensitive to small thruster faults.

Note that the occurrence of incipient or small size thruster faults (e.g., small propellant leakage or thrust loss) may be covered by (robust) control actions, and the early detection of them is clearly

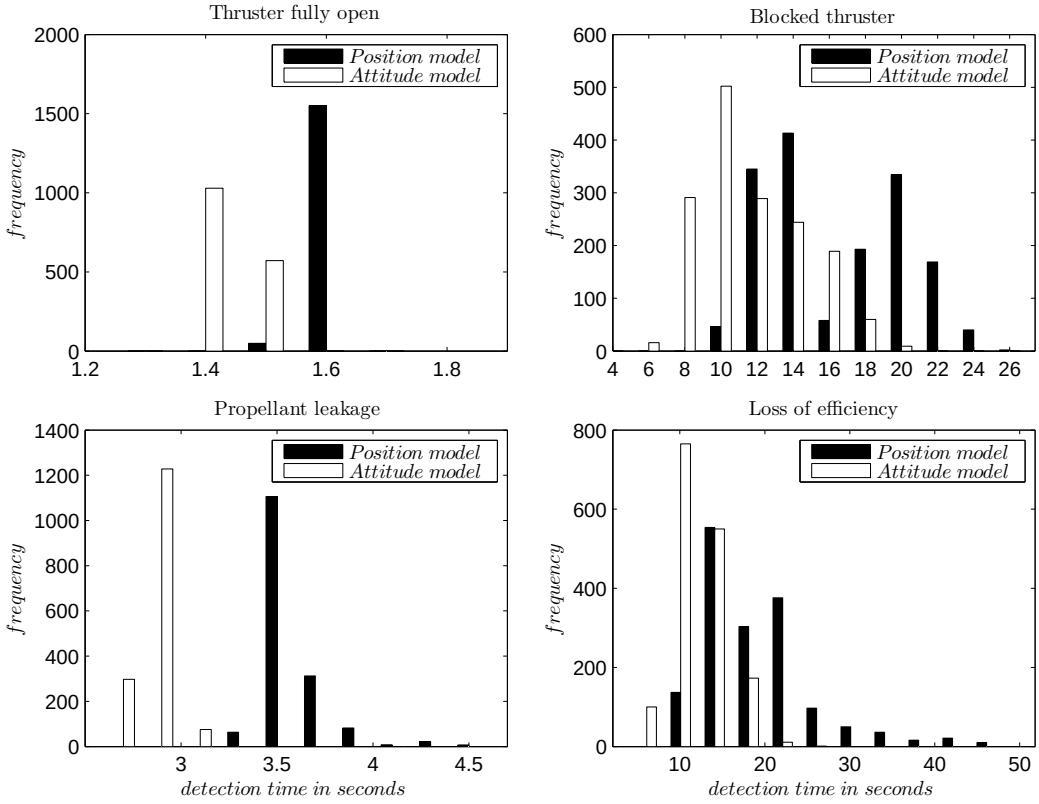

Fig. 11 Histograms of the detection times for the considered fault cases.

more difficult. Another problem can arise when a blocked-closed thruster is not commanded and thus a fault detection is almost impossible. Such behaviour was not observed, since the TMF respects the thruster non-linearities (minimum On/Off times) of each thruster.

By closer examining Fig. 12, it can be further observed that the final performances (isolation times) of both FDI schemes are only slightly different from each other. Note that the position model-based FDI unit succeeds thanks to the judiciously chosen linear model, i.e., a model which takes into account both the rotational and translational motions of the chaser. In other words, the dynamics of the attitude of the chaser is not modeled, but the chaser's quaternion is introduced in the residual computation. This allows to propose a fault diagnosis solution with a very similar performances to those based on the attitude model. Moreover, the position model is naturally robust against the model uncertainties, such as center of mass and inertia whilst the attitude model not. The linearity of the attitude model during the fault presence is questionable.

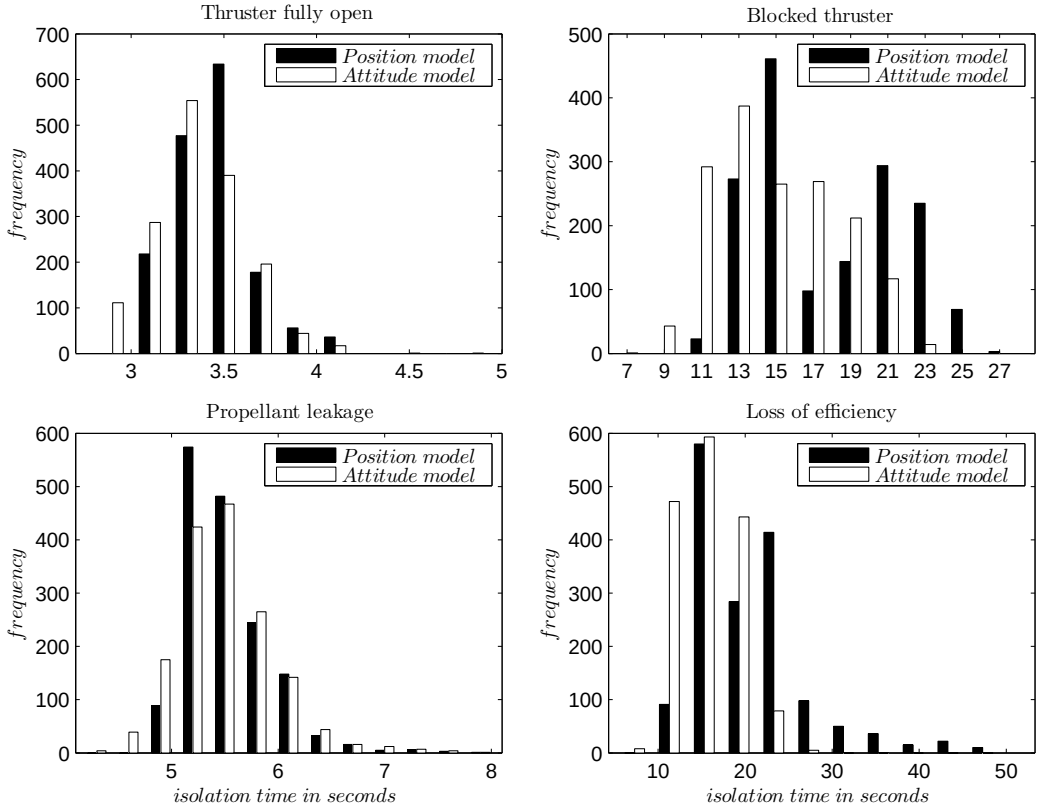

Fig. 12 Histograms of the isolation times for the considered fault cases.

VI. Conclusion

Design and implementation of two distinct model-based FDI strategies for thruster fault diagnosis of an autonomous spacecraft involved in the rendezvous phase of the MSR mission has been presented. Effects of unknown time-varying delays induced by the propulsion drive electronics and uncertainties on thruster rise times has been transformed into unknown input vector using Cayley-Hamilton theorem and h-order Taylor expansion. The estimation of the complex unknown input distribution matrix can be considered as a contribution to the theory. The robust (in the sense of unknown input decoupling) residual generation for FDI has been achieved using observer eigenstructure assignment technique, i.e., some left eigenvectors of the observer have been assigned to be orthogonal to the unknown input directions (columns of the distribution matrix). Thruster fault isolation has been achieved by cross-correlation test between the residual signal and the commanded thruster open durations. The core element of this study is the judiciously chosen position model. This model has been used to design the first FDI scheme and was compared (in terms of

well established FDI performance indices) to the second, attitude model-based, scheme. A Monte Carlo simulation campaign, using a "high-fidelity" industrial simulator, has been performed under realistic conditions, considering imperfect navigation, delays, spatial disturbances and parameter uncertainties. Four different fault scenarios were injected throughout simulations. Obtained results indicate, that the proposed FDI strategies are effective and applicable for on-board implementation. Moreover, the selected performance indices reveal, that the position model-based scheme tends to achieve very similar FDI performances as the scheme based on the pure attitude model.

Appendix A: Uncertainty Transformation Using Cayley-Hamilton Theorem

Let us first consider the following theorem [46]:

Theorem 2. The characteristic polynomial of matrix $\boldsymbol{A}$ is

$$p(\lambda) = \det(\lambda \boldsymbol{I} - \boldsymbol{A}) = \lambda^{n_x} + c_{n-1}\lambda^{n_x-1} + \ldots + c_1\lambda + c_0 \tag{46}$$

then $e^{\boldsymbol{A}t}$ can be written as

$$e^{\boldsymbol{A}t} = s_1(t)\boldsymbol{I} + s_2(t)\boldsymbol{A} + \ldots + s_{n_x}(t)\boldsymbol{A}^{n_x-1} \tag{47}$$

where $s_i(t)$, $1 \leq i \leq n_x$ are solutions to the nth order homogenous scalar differential equation

$$s^{(n_x)}(t) + c_{n_x-1}s^{(n_x-1)}(t) + \ldots + c_1 s'(t) + c_0 s(t) = 0 \tag{48}$$

satisfying the following initial conditions

$$s_i^{(i-1)}(0) = 1, \;\; s_i^{(j)}(0) = 0 \;\; \text{for} \;\; j \neq i-1, 0 \leq j \leq n_x - 1$$

The proof of this theorem can be found in [46].

Using (47), we have

$$\boldsymbol{\Gamma}_1^a(\delta(k)) = \int_{T-\delta(k)}^{T} e^{\boldsymbol{A}t} dt \boldsymbol{B} = \sum_{i=1}^{n_x} \left[\left(\int_{T-\delta(k)}^{T} s_i(t)dt \right) \boldsymbol{A}^{i-1}\boldsymbol{B} \right] \tag{49}$$

Define

$$s_i^{\max} = \max_{0 \leq \delta(k) \leq T} \int_{T-\delta(k)}^{T} s_i(t)dt, \quad i = 1, 2, \ldots, n_x$$

$$s_i^{\min} = \min_{0\le\delta(k)\le T} \int_{T-\delta(k)}^{T} s_i(t)dt, \quad i = 1, 2, \ldots, n_x$$

then (49) can be rewritten as

$$\boldsymbol{\Gamma}_1^a(\delta(k)) = \sum_{i=1}^{n_x} \left(\alpha_{i,0}(k)s_i^{\min} + \alpha_{i,1}(k)s_i^{\max}\right) \boldsymbol{A}^{i-1}\boldsymbol{B} \tag{50}$$

where $\alpha_{i,0}(k)$ and $\alpha_{i,1}(k)$ are two time-varying unknown parameters satisfying $0 \le \alpha_{i,0}(k) \le 1$, $0 \le \alpha_{i,1}(k) \le 1$, and $\alpha_{i,0}(k) + \alpha_{i,1}(k) = 1$ for $\forall k \in \mathbb{Z}^+$. It can be verified that $\int_{T-\delta(k)}^{T} s_i(t)dt, i = 1, 2, \ldots, n_x$ are Lipschitz-continuous on $0 \le \delta(k) \le T$, i.e., they satisfy

$$\left| \int_{T-\delta_1(k)}^{T} s_i(t)dt - \int_{T-\delta_2(k)}^{T} s_i(t)dt \right| \le \kappa_i \left|\delta_1(k) - \delta_2(k)\right|$$

$\forall \delta_1(k), \delta_2(k) \in [0, T]$, where $\kappa_i, i = 1, 2, ..., n_x$ are the Lipschitz constants.

Setting

$$\begin{aligned} \mu_{2i-1}^a(k) &= \alpha_{i,0}(k)/n_x, \qquad & \boldsymbol{U}_{2i-1}^a &= n_x s_i^{\min}\boldsymbol{A}^{i-1}\boldsymbol{B} \\ \mu_{2i}^a(k) &= \alpha_{i,1}(k)/n_x, & \boldsymbol{U}_{2i}^a &= n_x s_i^{\max}\boldsymbol{A}^{i-1}\boldsymbol{B} \end{aligned} \tag{51}$$

then Eq. (24) in proposition 1 yields Eq. (50).

Appendix B: Uncertainty Transformation Using Taylor Series Expansion

Theorem 3. Taylor series expansion of the uncertainty $\boldsymbol{\Gamma}_1(\delta(k))$ is given by

$$\boldsymbol{\Gamma}_1^b(\delta(k)) = -\sum_{i=1}^{\infty}(-\delta(k))^i \frac{\boldsymbol{A}^{i-1}}{i!} e^{\boldsymbol{A}T}\boldsymbol{B}$$

The h-order approximation of Taylor expansion for the uncertainty $\boldsymbol{\Gamma}_1(\delta(k))$ can be expressed as a finite sum of the first h elements

$$\boldsymbol{\Gamma}_1^b(\delta(k)) = -\sum_{i=1}^{h}(-\delta(k))^i \frac{\boldsymbol{A}^{i-1}}{i!} e^{\boldsymbol{A}T}\boldsymbol{B}$$

Consider $\underline{\varepsilon} = \delta_{min}$, $\overline{\varepsilon} = \delta_{max}$ and $\varepsilon \in [\underline{\varepsilon}, \overline{\varepsilon}]$. Now setting

$$\begin{aligned} &\mu_1(k) = 1 - \tfrac{\varepsilon(k)-\underline{\varepsilon}}{\overline{\varepsilon}-\underline{\varepsilon}}, \\ &\mu_i(k) = \tfrac{\varepsilon^{i-1}(k)-\underline{\varepsilon}^{i-1}}{\overline{\varepsilon}^{i-1}-\underline{\varepsilon}^{i-1}} - \tfrac{\varepsilon^{i}(k)-\underline{\varepsilon}^{i}}{\overline{\varepsilon}^{i}-\underline{\varepsilon}^{i}}, \quad i = 2, \ldots, h \\ &\boldsymbol{U}_i^b = \left[\, \boldsymbol{G}_h, \ \ldots \ , \boldsymbol{G}_1 \,\right] \boldsymbol{\Phi}_i, \quad i = 1, \ldots, h+1 \end{aligned} \tag{52}$$

where

$$\boldsymbol{G}_i = (-1)^{i+1}\frac{\boldsymbol{A}^{i-1}}{i!}e^{\boldsymbol{A}T}\boldsymbol{B},\ i = 1, \ldots, h$$

$$\boldsymbol{\Phi}_1 = \left[\begin{array}{cccccc} \underline{\varepsilon}^h\boldsymbol{I} & \underline{\varepsilon}^{h-1}\boldsymbol{I} & , ..., & \underline{\varepsilon}^2\boldsymbol{I} & \underline{\varepsilon}\boldsymbol{I} \end{array}\right]^T$$

$$\boldsymbol{\Phi}_2 = \left[\begin{array}{cccccc} \underline{\varepsilon}^h\boldsymbol{I} & \underline{\varepsilon}^{h-1}\boldsymbol{I} & , ..., & \underline{\varepsilon}^2\boldsymbol{I} & \overline{\varepsilon}\boldsymbol{I} \end{array}\right]^T$$

$$\vdots$$

$$\boldsymbol{\Phi}_{h+1} = \left[\begin{array}{cccccc} \overline{\varepsilon}^h\boldsymbol{I} & \overline{\varepsilon}^{h-1}\boldsymbol{I} & , ..., & \overline{\varepsilon}^2\boldsymbol{I} & \overline{\varepsilon}\boldsymbol{I} \end{array}\right]^T$$

then using h-order Taylor expansion, Eq. (52) yields Eq. (25) given in proposition 2. This proposition is proved in [40].

Acknowledgments

This research work was supported by the European Space Agency (ESA) and Thales Alenia Space France in the frame of the ESA Networking/Partnering Initiative (NPI) program.

References

[1] Osder, S.,"Practical View of Redundancy Management Application and Theory," *Journal of Guidance, Control, and Dynamics*, Vol. 22, No. 1, 1999, pp. 12–21. doi: 10.2514/2.4363

[2] Olive, X., "FDI (R) for satellites: How to deal with high availability and robustness in the space domain?," *International Journal of Applied Mathematics and Computer Science*, Vol. 22, No. 1, 2012, pp. 99–107. doi: 10.2478/v10006-012-0007-8

[3] Zolghadri, A., "Advanced Model-Based FDIR Techniques for Aerospace Systems: Today Challenges and Opportunities," *Progress in Aerospace Sciences*, Vol. 53, No. 3, 2012, pp. 18–29. doi: 10.1016/j.paerosci.2012.02.004

[4] Peuvédic, C. L., Colmenarejo, P., and Guiotto, A., "Autonomous Rendezvous Control System: a High Fidelity Functional Engineering Simulator Developed for GNC/AMM/FDIR Validation," *Proceeding of the 7th International ESA Conference on Guidance, Navigation and Control Systems*, Tralee, County Kerry, Ireland, Jun. 2008.

[5] Strippoli, L. et. al., "Integrated vision-based GNC for Autonomous Rendezvous and Capture around Mars," *9th International ESA Conference on Guidance, Navigation & Control Systems*, Porto, Portugal, Jun. 2014.

[6] Isermann, R., "Model-Based Fault Detection and Diagnosis - Status and Applications," *Annual Reviews in Control*, Vol. 29, No. 1, 2005, pp. 71–85. doi: 10.1016/j.arcontrol.2004.12.002

[7] Venkatasubramanian, V., Rengaswamy, R., Yin, K., and Kavuri, S. N., "A Review of Process Fault Detection and Diagnosis: Part I: Quantitative Model-Based Methods," *Computers & Chemical Engineering*, Vol. 27, No. 3, 2003, pp. 293–311. doi: 10.1016/S0098-1354(02)00160-6

[8] Henry, D., Simani, S., and Patton, R., "Fault Detection and Diagnosis for Aeronautic and Aerospace Missions," *Fault Tolerant Flight Control: A Benchmark Challenge*, Springer Verlag, Berlin/Heidelberg, 2010, pp 91–128.

[9] Zolghadri, A., Henry, D., Cieslak, J., Efimov, D., and Goupil P., *Fault Diagnosis and Fault-Tolerant Control and Guidance for Aerospace Vehicles*, Springer Verlag, London, 2014, Chap. 7.

[10] Chen, W., and Saif, M., "Observer-Based Fault Diagnosis of Satellite Systems Subject to Time-Varying Thruster Faults," *Journal of Dynamic Systems, Measurement and Control*, Vol. 129, No. 3, 2007, pp. 352–356. doi:10.1115/1.2719773

[11] Patton, R., Uppal, F., Simani, S., and Polle, B., "Reliable Fault Diagnosis Scheme for a Spacecraft Attitude Control System" *Journal of Risk and Reliability*, Vol. 222, No. 2, 2008, pp. 139–152. doi: 10.1243/1748006XJRR98

[12] Patton, R., Uppal, F., Simani, S., and Polle, B., "Robust FDI Applied to Thruster Faults of a Satellite System," *Control Engineering Practice*, Vol. 18, No. 9, 2010, pp. 1093–1109. doi: 10.1016/j.conengprac.2009.04.011

[13] Henry, D., "Fault Diagnosis of Microscope Satellite Thrusters Using H_∞/H_- Filters," *AIAA Journal of Guidance, Control, and Dynamics*, Vol. 31, No. 3, 2008, pp. 699–711. doi: 10.1109/TSMCA.2010.2063022

[14] Falcoz, A., Boquet, F., and Flandin, G., "Robust H_∞/H_- Thruster Failure Detection and Isolation with Application to the LISA Pathfinder Spacecraft," *AIAA Guidance, Navigation, and Control Conference*, AIAA Paper 2010–7906, Toronto, Ontario, Aug. 2010.

[15] Yang H., and Saif, M., "Observer Design and Fault Diagnosis for State-Retarded Dynamical Systems," *Automatica*, Vol. 34, No. 2, 1998, pp. 217–227. doi: 10.1016/S0005-1098(97)00175-1

[16] Kratz, F., Nuninger, W., and Ploix, S., "Fault Detection for Time-Delay Systems: A Parity Space Approach," *Proceedings of the American Control Conference*, Vol. 4, Philadelphia, PA, Jun 1998, pp. 2009–2011.

[17] Ding, S. X., Maiying, Z., Bingyong, T., and Zhang, P., "An LMI Approach to the Design of Fault Detection Filter for Time-Delay LTI Systems with Unknown Inputs," *Proceedings of the American*

Control Conference, Vol. 3, Arlington, VA, Jun 2001, pp. 2137–2142. doi: 10.1109/ACC.2001.946063

[18] Jiang, B., Staroswiecki, M., and Cocquempot, V., "H_∞ Fault Detection Filter Design for Linear Discrete-Time Systems with Multiple Time Delays," *International Journal of System Science*, Vol. 34, No. 5, 2003, pp. 365–373. doi: 10.1080/00207720310001601037

[19] Jiang, C., and Zhou, D. H., "Fault Detection and Identification for Uncertain Linear Time-Delay Systems," *Computers and Chemical Engineering*, Vol. 30, No. 2, 2005, pp. 228–242. doi: 10.1016/j.compchemeng.2005.08.012

[20] Meskin, N., and Khorasani, K. "Robust Fault Detection and Isolation of Time-Delay Systems Using a Geometric Approach," *Automatica*, Vol. 45, No. 6, 2009, pp. 1567–1573. doi: 10.1016/j.automatica.2009.02.019

[21] Karimi, H. R., Zapateiro, M., and Luo, N., "A Linear Matrix Inequality Approach to Robust Fault Detection Filter Design of Linear Systems with Mixed Time-Varying Delays and Nonlinear Perturbations," *Journal of the Franklin Institute*, Vol. 347, No. 6, 2010, pp. 957–973. doi: 10.1016/j.jfranklin.2010.03.004

[22] Patton, R. J., and Chen, J., "Robust Fault Detection of Jet Engine Sensor Systems Using Eigenstructure Assignmen," *Journal of Guidance, Control, and Dynamics*, Vol. 15, No. 6, 1992, pp. 1491–1497. doi: 10.2514/3.11413

[23] Patton, R. J., Willcox, S. W., and Winter, J. S., "Parameter-Insensitive Technique for Aircraft Sensor Fault Analysis," *Journal of Guidance, Control, and Dynamics*, Vol. 10, No. 4, 1987, pp. 359–367. doi: 10.2514/3.20226

[24] Fonod, R., Henry, D., Charbonnel, C., and Bornschlegl, E., "Robust Thruster Fault Diagnosis: Application to the Rendezvous Phase of the Mars Sample Return Mission," *2nd CEAS Specialist Conference on Guidance, Navigation and Control*, Delft, Netherlands, Apr. 2013.

[25] Fonod, R., Henry, D., Bornschlegl, E., and Charbonnel, C., "Robust Fault Detection for Systems with Electronic Induced Delays: Application to the Rendezvous Phase of the MSR Mission," *European Control Conference*, Zurich, Switzerland, Jul. 2013.

[26] D'Amario, L. A., et al. "Mars Orbit Rendezvous Strategy for the Mars 2003/2005 Sample Return Mission," *AAS/AIAA, Astrodynamics Specialist Conference*, AIAA Paper 99–306, Girdwood, AK, Aug. 1999.

[27] Cazaux, C., et al. "The NASA/CNES Mars Sample Return - A Status Report," *Acta Astronautica*, Vol. 54, No. 8, 2004, pp. 601–617. doi: 10.1016/j.actaastro.2003.07.001

[28] Beaty, D., Grady, M., May, L., and Gardini, B., "Preliminary planning for an international Mars Sample Return mission," *Report of the International Mars Architec-*

ture for the Return of Samples (iMARS) Working Group, Jun. 2008. Available from: <http://mepag.jpl.nasa.gov/reports/iMARS_FinalReport.pdf>

[29] Peuvédic, C. L., Maini, M., Lafontaine, J. D., Kron, A., and Ortega, G., "Key Control Techniques for GNC Design of Martian Vehicles," *6th International ESA Conference on Guidance, Navigation and Control Systems*, Loutraki, Greece, Oct. 2005.

[30] Pettazzi, L., Lanzon, A., Theil, S., and Finzi, A. E., "Design of Robust Drag-Free Controllers with Given Structure," *Journal of Guidance, Control, and Dynamics*, Vol. 32, No. 5, 2009, pp. 1609–1621. doi: 10.2514/1.40279

[31] Pelletier, F., Golla, D., and Allen, A., "Lidar-Based Rendezvous Navigation for MSR," *AIAA Guidance, Navigation, and Control Conference*, AIAA Paper 2004–4987, Providence, Rhode Island, Aug. 2004.

[32] Issury, I., Henry, D., Charbonnel, C., Bornschlegl, E., and Olive, X., "A Boolean Algebraic-Based Solution for Multiple Fault Diagnosis: Application to a Spatial Mission," *Aerospace Science and Technology*, Vol. 28, No. 1, 2013, pp. 214–226. doi: 10.1016/j.ast.2012.11.002

[33] Wie, B., *Space vehicle dynamics and control*, AIAA Education Series, Reston, VA, 1998, Chap. 5.

[34] Schaub, H., and Junkins, J. L., *Analytical Mechanics of Space Systems*, AIAA Education Series, New York, NY, 2003, Chap. 13.

[35] Clohessy, W. H., and Wiltshire, R. S., "Terminal Guidance System for Satellite Rendezvous," *Journal of the Aerospace Sciences*, Vol. 27, No. 9, 1960, pp. 653–658. doi: 10.2514/8.8704

[36] Frank, P. M., Alcorta-Garcia, E., and Köppen-Seliger, B., "Modelling for Fault Detection and Isolation versus Modelling for Control," *Mathematical and Computer Modelling of Dynamical Systems*, Vol. 7, No .1, 2001, pp. 1–46. doi: 10.1076/mcmd.7.1.1.3633

[37] Wertz, J. R., *Spacecraft Attitude Determination and Control*, D. Reidel Publishing Company, Boston, AM, Vol. 73, 1978, Chap. 16.

[38] Massoumnia, M. A., "A Geometric Approach to the Synthesis of Failure Detection Filters," *IEEE Transactions on Automatic Control*, Vol. 31, No. 9, 1986, pp. 839–846. doi: 10.1109/TAC.1986.1104419

[39] Wang, Y., Ding, S. X., Ye, H., and Wang, G., "A New Fault Detection Scheme for Networked Control Systems Subject to Uncertain Time-Varying Delay," *IEEE Transactions on Signal Processing*, Vol. 56, No. 10, 2008, pp. 5258–5268. doi: 10.1109/TSP.2008.928703

[40] Hetel, L., Daafouz, J., and Iung, C., "Stabilization of Arbitrary Switched Linear Systems with Unknown Time-Varying Delays," *IEEE Transactions on Automatic Control*, Vol. 51, No. 10, 2006, pp. 1668–1674. doi: 10.1109/TAC.2006.883030

[41] Ding, S. X., Jeinsch, T., Frank, P. M., and Ding, E. L., "A Unified Approach to the Optimization of

Fault Detection Systems," *International Journal of Adaptive Control and Signal Processing*, Vol. 14, No. 7, 2000, pp. 725–745.

[42] Chen J., and Patton, R., *Robust model-based fault diagnosis for dynamic systems*, Kluwer Academic Publishers, Dordrecht, 1999, Chap. 4.

[43] Ding, S. X., *Model-Based Fault Diagnosis Techniques: Design Schemes, Algorithms, and Tools*, Springer Verlag, New York, 2008, Chap. 10.

[44] Basseville, M., and Nikiforov, I. V., *Detection of Abrupt Changes: Theory and Application*, Prentice Hall, Englewood Cliffs, NJ, 1993, Chap. 10.

[45] Frank, P. M., "Fault Diagnosis in Dynamic Systems Using Analytical and Knowledge-Based Redundancy: A Survey and Some New Results," *Automatica*, Vol. 26, No. 3, 1990, pp. 459–474. doi: 10.1016/0005-1098(90)90018-D

[46] Leonard, I. E., "The Matrix Exponential," *SIAM review*, Vol. 38, No. 3, 1996, pp. 507–512. doi: 10.1137/S0036144595286488